Spitzer Space Telescope Observations of Kepler's Supernova Remnant: A Detailed Look at the Circumstellar Dust Component[1]

William P. Blair[2], Parviz Ghavamian[2], Knox S. Long[3], Brian J. Williams[4], Kazimierz J. Borkowski[4], Stephen P. Reynolds[4] & Ravi Sankrit[5]

ABSTRACT

We present 3.6 - 160 μm infrared images of Kepler's supernova remnant (SN1604) obtained with the IRAC and MIPS instruments on the *Spitzer Space Telescope*. We also present MIPS SED low resolution spectra in the 55 - 95 μm region. The observed emission in the MIPS 24 μm band shows the entire shell. Emission in the MIPS 70 μm and IRAC 8 μm bands is seen only from the brightest regions of 24 μm emission, which also correspond to the regions seen in optical Hα images. Shorter wavelength IRAC images are increasingly dominated by stars, although faint filaments are discernible. The SED spectrum of shows a faint continuum dropping off to longer wavelengths and confirms that strong line emission does not dominate the mid-IR spectral region. The emission we see is due primarily to warm dust emission from dust heated by the primary blast wave; no excess infrared emission is observed in regions where supernova ejecta are seen in X-rays. We use models of the dust to interpret the observed 70/24 μm ratio and constrain the allowed range of temperatures and densities. We estimate the current mass of dust in the warm dust component to be 5.4×10^{-4} $M_{\odot}$, and infer an original mass of about 3×10^{-3} $M_{\odot}$ before grain sputtering. The MIPS 160 μm band shows no emission belonging to the remnant. We place a conservative but temperature dependent upper limit on any cold dust component roughly a factor of 10 below the cold dust mass inferred from SCUBA observations. Finally,

[1]Based on observations made with the NASA *Spitzer* Space Telescope. *Spitzer* is operated for NASA by the Jet Propulsion Lab.

[2]Department of Physics & Astronomy, Johns Hopkins University, 3400 North Charles Street, Baltimore, MD 21218

[3]Space Telescope Science Institute, 3700 San Martin Drive, Baltimore, MD 21218

[4]Department of Physics, North Carolina State University, Raleigh, NC 27695-8202

[4]Space Sciences Laboratory, University of California Berkeley, Berkeley, CA 94720-7450

we comment on issues relevant to the possible precursor star and the supernova type.

Subject headings: ISM: individual (SN 1604) — ISM: dust — ISM: nebulae — ISM: supernova remnants — Shock waves

1. Introduction

Each of the remnants of historical galactic supernovae (SNe) provides a unique and important perspective to our understanding of young supernova remnants (SNRs) and their interaction with the interstellar medium (ISM). SN 1604 is the second youngest galactic SNR (behind Cas A), and was first sighted in October 1604 by Johannes Kepler and others. Kepler was not the first to see the SN, but he published the most detailed account of the SN light curve (Kepler 1606), and largely because of this the SNR has come to be known as Kepler's SNR. Baade (1943) was the first to recover the optical SNR. It has been well observed at all wavelengths (X-ray: Cassam-Chenaï et al. 2004, Hughes 1999; Radio: DeLaney et al. 2002; Optical: Blair et al. 1991, Sollerman et al. 2003; NIR/IR: Gerardy & Fesen 2001, Douvion et al. 2001; sub-mm: Morgan et al. 2003; and numerous earlier papers referenced therein).

The distance to Kepler's SNR has been uncertain, with most investigators adopting a value of near 5 kpc, as discussed by Reynoso & Goss (1999). However, Kepler's SNR lies almost directly toward the galactic center, making the use of H I velocities and a galactic rotation curve very unreliable. Using an HST/ACS image compared to ground-based data, Sankrit et al. (2005) have recently determined a distance of 3.9 (+1.9, -1.4) kpc to Kepler using the proper motion of a filament whose velocity is known with reasonable accuracy (Blair et al. 1991). Since the uncertainty is still rather large, we will adopt a value of 4 kpc in this paper and scale other parameters to this value. The SNR lies 6.8° off the galactic plane (473 d_4 pc). With an angular diameter of ∼200″, the radius is 1.93 d_4 pc and the mean expansion velocity has been ∼ 4720 d_4 km s^{-1}. Since the current velocity of the primary blast wave is ∼1660 ±120 km s^{-1} (Blair et al. 1991; Sankrit et al. 2005), the primary shock has been significantly decelerated over 400 years.

The brightest optical emission is from a region in the WNW, as shown in the images of Blair et al. (1991). Bright [S II] emission indicates slower, denser, radiative shocks. However, more extensive nonradiative emission is present where smoother Hα filaments are not accompanied by [S II], for instance, across the N rim and in portions of two centrally-projected regions. We shall refer frequently below to the different character of the radiative and nonradiative emission regions.

Douvion et al. (2001) observed Kepler with the ISOCAM instrument aboard the Infrared Space Observatory (ISO), with an angular resolution of 6″, in a band from 10.7 – 12.0 μm. Spectra were also obtained between 6.5 and 16 μm. They found the emission to have a similar morphology to the Hα image, but made no distinction between radiative and non-radiative regions. They found almost no line emission to be present and were able to fit their spectra with collisionally heated dust at a fixed temperature, using "astronomical silicate" composition (Draine & Lee 1984), assuming that dust was heated in regions with densities and temperatures consistent with radiative shock emission ($n_e \sim (2-10)\times10^3$ cm^{-3}, $T_e \sim 10^4$ K. They reported a total dust mass of order 10^{-4} $M_\odot$.

Kepler's SNR is the only of the historical SNe from the last millennium whose progenitor type is a matter of serious debate (Blair 2005). The early claim by Baade (1943) of consistency of the historical light curve with a Type Ia SN has been questioned by Doggett & Branch (1985) and Schaefer (1996) among others. The presence of dense, (apparently) N-rich circumstellar material (CSM) surrounding the SNR so high off the galactic plane was taken to indicate pre-SN mass loss from a massive star and hence a core collapse SN (Bandiera 1987). The progenitor could have been a runaway star, which is consistent with the observed morphology (Borkowski et al. 1992; 1994; Velázquez et al. 2006). On the other hand, analyses of X-ray spectra from Exosat (Decourchelle & Ballet 1994), ASCA (Kinugasa & Tsunemi 1999, 2000) and more recently XMM-Newton (Cassam-Chenaï et al. 2004) indicate an overabundance of Fe and Si enhanced ejecta, which is not expected from the explosion of a massive star but instead suggests a Type Ia designation.

At some point in the evolution of a young SNR, some of the SN ejecta may form into interstellar dust of various types, depending on the SN type (e.g. Arendt et al. 1999). Evidence exists for the formation of dust on 1-2 year time scales in core-collapse SN (SN 1987A–McCray 1993 and Bouchet et al. 2004; SN 1999em–Elmhamdi et al. 2003). The large mass of iron produced by Type Ia SNe suggests that grains may form there as well, although direct evidence for this process is scant and timescales are not well known. Dunne et al. (2003) have reported the detection of a large mass of very cold dust in Cas A based on SCUBA (sub-mm) observations, although these conclusions have been called into question (Dwek 2004a,b; Krause et al. 2004). Morgan et al. (2003) have reported SCUBA observations of Kepler's SNR and claimed a large mass of cold (17 K) dust. A SN blast wave sweeps up gas and dust as it expands, and so any circumstellar or interstellar dust should also be heated, and ultimately sputtered and destroyed by collisions in the post shock region. Hence, young SNRs can in principle be dust-processing laboratories. With the advent of the *Spitzer Space Telescope*, it is possible to study these effects in unprecedented detail.

Spitzer observations of Magellanic Cloud SNRs are shedding some light on these issues.

Borkowski et al. (2006) looked exclusively at four remnants of Type Ia SNe. They found no evidence of dust from the ejecta, but rather emission consistent with heating of ISM dust by the expanding blast wave. B. Williams et al. (2006) selected a group of suspected remnants of core collaspe SNe in the LMC and have found similar results: no obvious dust emission associated with regions of ejecta but dust emission associated with the primary blast wave was prominent. R. Williams et al. (2006) report *Spitzer* observations of a different sample of LMC SNRs and suggest that, at least in some objects, line emission may dominate over the dust continuum. However, even in these objects, the emission arises at positions consistent with shocked ISM.

In this paper, we report infrared imaging and spectroscopy of Kepler's SNR using the MIPS and IRAC instruments on *Spitzer*, obtained as part of a Cycle 1 Guest Observer program (#3413). We find evidence for swept-up dust heated by the primary blast wave, but do not see evidence for the cold dust component reported by Morgan et al. (2003). Modeling of the dust and comparison to observed ratios are used to constrain the allowed plasma conditions in the shocked gas.

2. Observations and Data Processing

Below we describe the *Spitzer* MIPS (Rieke et al. 2004) and IRAC (Fazio et al. 2004) imaging and present the data. The MIPS instrument also has a low resolution spectral energy distribution (SED) spectroscopy mode, and the data obtained on Kepler are described in the subsequent sub-section.

2.1. *Spitzer* Imaging

We observed Kepler's SNR using MIPS imaging at 24, 70 and 160 μm, and with all four bands of IRAC (3.6, 4.5, 5.8 and 8.0 μm). All MIPS photometric imaging used the 'small' field size. The 160 μm band should be most sensitive to the distribution of cold dust, being near the peak of the curve fit by Morgan et al. (2003) to the SCUBA data. Based on the ISO measurements of Douvion et al. (2001), the 24 and 70 μm MIPS bands and 8 μm IRAC band should assess the warmer dust component near 120 K.

At 24 μm we used one cycle and no mapping with a 10 s exposure time. The 70 μm band used 10 s exposure times, 1 cycle and a 3x1 map for two cycles (step size at 1/2 array for columns and full array for rows). This results in 252 sec integration time and covers the object with room to spare to assess background, and enough overlap to account for the

side B problem. The smaller FOV of the 160 μm band (along with the anomalous block of 5-pixels) required a greater number of positions to cover the desired region. We chose 10 sec exposures and 4 cycles. We then chose mapping with 1x3 for 3 map cycles. This results in an integration time of 252 sec.

We worked with the standard post-BCD reduction data sets for the MIPS imaging data, as retrieved with `Leopard` from the *Spitzer* archive. The data have been reprocessed several times over the course of this work, and here we report the S11.0.2 version of the processed data. Figure 1 shows the full field of view MIPS 24 μm image, which is by far the most sensitive and detailed of the *Spitzer* images obtained.

Kepler fits within a single IRAC field. Our AOR used the 12 position Reuleaux dither pattern and 2-100 sec frames per pointing to to achieve a 2400 sec integration time in all four bands. We again worked with the post-BCD data sets, which were processed with version S11.4.0. While some SNR emission is apparent in the 8 μm image, it is difficult to assess the shorter wavelength IRAC images for SNR emission because of stellar contamination.

Hence, to better investigate the extent of SNR emission in the IRAC bands, we have displayed these data in two ways. First, we made three-color images. Figure 2a shows a three-color IRAC image with 8 μm (red), 5.6 μm (green), and 3.6 μm (blue). Stars are white or bluish and the SNR emissions appear orange and yellow. Orange filaments show emission at both 8.0 and 5.6 μm, but are dominated by the longer wavelength band. Yellow filaments appear to correspond closely with the brighter radiative filaments and indicate relatively stronger emission at 5.6 μm. Any SNR emission at 3.6 μm is completely dominated by the longer wavelengths. Figure 2b shows a similar comparison, but using 5.6 μm as red, 4.5 μm in green and again 3.6 μm in blue. Even more so than Fig. 2a, this combination shows only emission from the densest (radiative) optical filaments, which appear as orange (indicating emission in both the 4.5 and 5.6 μm bands). The two patches of green emission in this Figure adjacent to bright stars indicate instrumental effects in the 4.5 μm image.

Secondly, we have made difference images of adjacent bands to minimize the effects of stellar contamination. Since SNR emission likely occurs in the band being used for subtraction, these images are not useful for quantitative analysis, but rather for highlighting the overall extent of detected emission. Fig. 2c shows the residual emission when the 5.6 μm band is subtracted from the 8 μm image, and Figure 2d shows 4.5 μm minus 3.6 μm. While some stellar residuals remain, these two panels confirm the discussion from the three-color Figures above: fairly extensive emission is present at 8μm, and only a few of the brightest clumpy filaments remain visible at 4.5 μm.

For comparison, we show a medium scaling of the MIPS 24 μm image in Figure 2e, and a

0.3 - 0.6 keV energy cut of archival *Chandra* soft X-ray data in Figure 2f. Comparing Figure 2c and 2e shows that the region visible at 8 μm corresponds very closely to the brightest regions in the 24 μm image. There is also tremendous similarity between the softest X-rays and the 8 μm image. Since the densest regions should be coolest, this confirms to first order that the brightest regions in the 8 and 24 μm images are largely due to higher densities at these locations.

In Figure 3, we show the MIPS data and some additional comparisons, all on the same scale as the panels of Figure 2. Figure 3a and 3b show hard and soft stretches of the 24 μm data, respectively, highlighting the faintest and brightest regions detected at 24 μm. The MIPS 70 μm data were reprocessed using the GeRT software available from the *Spitzer* Science Center web site in an attempt to minimize the obvious striping that traverses these data from NNE to SSW. This made a modest improvement in the cosmetic appearance of the 70 μm image, but the original data set was used for all measurements reported in this paper. The corrected data are shown in Figure 3c. Although the resolution is lower at 70 μm, it is quite clear that the regions brightest at 70 μm correspond closely to the brightest emission at 24 μm. Figure 3d shows the star-subtracted Hα image from Blair et al. (1991). The overall extent of the Hα emission is quite silimar to the brightest infrared regions, although differences are apparent in the brightest region of radiative filaments in the WNW. Figure 3e shows the MIPS 160 μm image of the same region as the other panels. No emission is detected above the complex and variable background at 160 μm. Finally, Figure 3f shows a three color rendition of the *Chandra* X-ray data. The red shows the same energy cut as in Figure 2f (0.3 - 0.6 keV), green is the energy band 0.75 - 1.2 keV, and blue is a band from 1.64 - 2.02 keV.

2.2. MIPS SED Spectroscopy

The MIPS SED spectroscopy mode covers the spectral region from 55 μm to 95 μm with a resolution of 15 - 25. The SED aperture covers a region $3.8' \times 0.32'$ and produces a two-dimensional spectral output file with 16 pixels in the spatial direction and 32 pixels in the dispersion direction. A grid of aperture positions covering Kepler's SNR and an adjacent sky region were observed on 25 Sep. 2005. The spectral grid used a $3'$ chop distance in the dispersion direction and an overlapping "a" and "b" position in the spatial direction, covering the northern 2/3rds of the shell (mapping with two overlapping columns and 7 rows). With five cycles, this provided $\sim$300 sec integration times per position.

The primary purpose of the SED spectra was to search for evidence that strong emission lines might be contaminating the broad band imaging, and thus affect their intercomparison.

The individual spectra are low in signal and so we chose to sum the data covering the bright NW quadrant of the remnant (grid positions 2b, 3b, 4b, and 5b), using the corresponding sky positions that were furthest removed from SNR emission (sky positions s4b, s5b, s6b and s7b). The aperture positions used are shown in Figure 4, projected onto the 24 μm image. After summing the object data and subtracting sky, it was clear from displaying the two-dimensional data that the strongest signal was in columns 8 - 12. We collapsed these four columns into the spectrum shown in Fig. 5, which represents the bright NW radiative filaments and a portion of the NW shell. Because of the relatively crude state of SED calibration and software for handling these data, we do not attempt quantitative fits to the resulting spectrum, but rather rely on it to provide a more general description of the mid-IR spectrum.

The SED spectrum is dominated by the tail of the warm dust continuum as it fades to longer wavelengths. There is no evidence at this spectral resolution for the [O I] 63.2 μm line predicted to be strong in radiative shock models. There may be some indication of the 88.3 μm line of [O III], but it does not dominate the spectrum. A similar bump near 75 μm may be due to [N II] 76.5 μm, which might be consistent with the N overabundance of the shell material as judged from optical spectra, although the wavelength agreement is not very good. In any event, since lines do not dominate in this spectral region where the dust continuum is relatively faint, it is unlikely that line contamination has a signficant effect on the observed 24 μm flux where the dust emission is much stronger.

This point is strengthened by an IRS spectrum of the NW region by Roellig & Onaka (2004). This spectrum shows a modest emission feature near 26 μm that they mark as [Fe II] but which may be a blend of this line with [O IV] 25.9 μm. However, this emission feature makes only a small contribution to the total flux in the 24 μm band. The IRS spectrum extends down to the IRAC range, showing the dust continuum almost disappearing. In the IRAC 8 μm bandpass, a moderately strong [Ar II] line appears at 7.0 μm, accounting for $\sim$ 20% of the total flux. Hence, this is potentially important in considering ratios between the 8 μm image and other bands, at least for the NW filaments where bright radiative emission is dominating (e.g. Blair et al. 1991).

3. Analysis and Modeling

3.1. Morphological Comparisons

What is the structure of Kepler's SNR in the infrared and how does it compare to images at other wavelengths? Although the effective resolutions in the various data sets are

different, they are close enough to allow some meaningful intercomparisons. The 24 μm data are the deepest of the *Spitzer* data. Scaling to show only the highest surface brightness features, the similarity of Fig. 3b to the IRAC 8 μm (Fig. 2c) and 70 μm (Fig. 3c) indicates to first order that the same regions dominate all three bands. The further similarity to the optical Hα image (Fig. 3d) and the softest band of X-ray emission (Fig. 2f and red band in Fig. 3f) is striking. Since the majority of the optical emission especially across the northern limb arises from nonradiative shocks associated with the primary blast wave, it is clear that the brightest 8 μm, 24 μm, and 70 μm emissions are associated with this same component. Hence, heating of dust in dense, swept up CSM/ISM is the dominant mechanism operating in Kepler's SNR.

The morphology of the WNW region including the primary region of bright radiative filaments contains some subtle but important effects. Careful comparison of Fig. 3b and Fig. 3d shows differences between the brightest 24 μm morphology and the chaotic, more extended emission seen in the Hα image. We suggest the 24 μm image is dominated by emission from the primary blast wave in the moderate density interclump gas, and not the slower radiative shocks in the very dense radiative knots, which are dominated by [S II], [N II], and [O III] line emission (e.g. Blair et al. 1991). The 8 μm image (Fig. 2c) looks intermediate between the 24 μm and Hα appearance, which is another indicator that line emission from the radiative shocks contributes somewhat at this wavelength, as indicated above in the discussion of the IRS spectrum.

The 24 μm image scaled to highlight the lowest surface brightness structures (Fig. 3a) is the only of the IR images with sufficient signal to show the entire outer shell of the SNR. A general similarity is seen with the 3-color X-ray image in Fig. 3f, with the exception of the extended 'ears' to the WNW and ESE. Similarities to the 6 cm VLA data are apparent (e.g. DeLaney et al. 2002), in particular in the south and along the eastern rim. However differences are also apparent, including a relatively higher IR surface brightness in the NW, along the northern rim, and across the projected middle. The 'ears' mentioned above are most apparent in the radio data.

The disagreement in appearance in the projected interior of the shell deserves specific comment. Here an important clue comes from the optical spectroscopy of these central filaments by Blair et al. (1991). The SE central grouping of filaments are significantly red-shifted and thus are a portion of the receding shell of the SNR. In comparison, the NW central filaments are blue-shifted and are part of the approaching shell of the SNR. These filaments have direct counterparts in the soft X-ray band, but the association with the higher energy X-ray bands is less clear. The approaching filaments have no counterpart in the radio data, and while there is faint radio emission at the projected position of the SE central

grouping of filaments, the morphologies are different. Hence, it is not clear whether any of the central radio emission is correlated with either the optical or bright IR emissions in these regions.

In Figure 6, we show a different kind of morphological comparsion. This color composite, star-subtracted image shows Kepler's SNR as viewed by NASA's three Great Observatories, with *Spitzer* 24 μm data in red, *Hubble* Hα in yellow, *Chandra* 0.3 - 1.0 keV emission in green, and harder 2 - 10 keV *Chandra* emission in blue. This image provides a combination of physical information and some subtle affects due to differing spatial resolution of the data sets used. The *Hubble* data have the highest spatial resolution, but highlight the fact that the optical emission arises in knotty, dense structures being encountered by the primary blast wave. These filaments are bathed in the glow of the IR component, which arises from dust heated by the blast wave. The X-ray emission in the north extends out to the optical limb and stops. The red rim around the top is largely an artifact of the lower resolution of the 24 μm data and the stretch applied to this component of the image. (As we indicated in the discussion above, the brightest 24 μm emission is coincident with the shock front position.) However, the larger extension of the red emission in the NW appears to be a real effect.

The distribution of the two X-ray components in Fig. 6 is quite interesting. The harder X-rays (blue) primarily arise in sychrotron emission at the shock front, and are seen most clearly along the southern and eastern limbs. The softer X-ray component is dominated by thermal emission from Si and Fe rich ejecta (e.g. Cassam-Chenaï et al. 2004). In the south, this component lies directly interior to the blue component. In the north, this component largely fills in between the northern limb emission and the centrally-projected emission regions. Note the distinct absence of red emission in the green regions, which indicates *no significant warm dust emission* coincident with regions of ejecta.

3.2. Derivation of IR Fluxes and Ratios

3.2.1. Total Fluxes at 24 μm and 70 μm

We now turn to more quantitative information, concentrating first on the 24 μm and 70 μm data sets, where contamination of the SNR emission by stars is not a significant problem. We derived the total fluxes at these two wavelengths using the following method. Because the post-BCD data are in units of MJy sr^{-1}, we extract regions of pixels corresponding to the object, and use the known post BCD pixel sizes (from the file headers) and number of pixels included in each region to scale appropriately to total fluxes. We similarly extract representative regions of background surrounding the SNR region (as allowed by field cov-

erage) and average these to determine the most appropriate overall background levels to subtract. Using this technique, we obtain total fluxes at 70 and 24 μm of 4.90 Jy and 9.5 Jy, respectively, and thus a ratio of 70/24 μm of 0.52.

Our total flux at 70 μm appears to disagree with published *IRAS* fluxes at 60 μm (range from 7.1 - 10.5 Jy), summarized by Saken et al. (1992, their Table 6), although our derived 24 μm flux lies within the range listed (8.1 - 11.7 Jy) at IRAS 25 μm. The apparent disagreement arises simply from the differing bandpasses used. Bandpasses for *IRAS* are broader than for *Spitzer*, and thus would encompass more flux at a given wavelength. To confirm this, we integrated the output spectrum from the dust model described below for the entire remnant over the *IRAS* 60 μm bandpass and obtained an "expected" 60 μm flux of $\sim$8 Jy. A corresponding exercise for the *Spitzer* 70 μm band predicts a flux of 5 Jy.

3.2.2. Flux Measurements for Regions

In addition to the total fluxes, we have determined the 24 and 70 μm fluxes for several sub-regions of the remnant to search for variations in these ratios that might arise due to different shock or other parameters. We have also measured fluxes from relevant regions of the IRAC 8 μm image, although stellar contamination is a more significant problem for these data. Figure 7 shows the extraction regions projected onto the relevant images. These figures also define the nomenclature we will use below to reference the regions.

Because *Spitzer*'s optics provide images at or near the diffraction limit for all wavelengths, the resolution in images from various instruments differs by roughly the ratio of wavelengths. The angular resolutions of various images range from 2″ at 8 μm, to 6.2″ at 24 μm, 18″ at 70 μm, and 41″ at 160 μm. For determination of flux ratios from various regions of the SNR, it is necessary to convolve the higher-resolution image of interest to the resolution of the lower-resolution image. For the 8/24 μm ratios, we convolve the 8 μm image to the resolution of that at 24 μm, and for the 24/70 μm ratios, we convolve the 24 μm image to the resolution of that at 70 μm. We used contributed software by K. Gordon (U. Arizona) distributed by the SSC to convolve the images, using kernels for convolving 24 μm images to the same PSF as 70 μm, and similarly for 8 μm to 24 μm. These kernels are slightly temperature-dependent; we used versions appropriate for 100 K. Though we do not expect blackbody spectral shapes, this value is close to the appproximate grain temperatures reported by Douvion et al. (2001). In each case, the higher-resolution images were resampled onto a grid identical to that of the lower resolution image, using AIPS (Astronomical Image

Processing System)[1] task HGEOM. These are the images shown in Figure 7.

The extraction regions were defined to select physically associated regions of emission so that the results could be compared. We displayed and aligned the 24 and 70 μm images using the display tool `ds9`. [2] We also displayed the optical Hα and other images on the same scale for reference and comparison while defining regions. The defined 24 and 70 μm regions are shown in Figure 7a-c, and details are given at the top of Table 1. Object position O1 enclosed the region of bright radiative emission in the NW, position O2 enclosed the entire bright NW rim at 24 μm. Note that by differencing these two positions, the area corresponding to just the relatively bright nonradiative portion of the NW rim can be extracted. O3 samples the northern (mainly) nonradiative rim, and O4 and O5 enclose the two centrally-projected regions of knotty filaments.

Background regions were identified to the north and south of the remnant to account for the gradient observed in the background from north to south. Some backgrounds were defined specifically for use with the 70 μm image in an attempt to better account for the significant striping in this image. For each object position, the most appropriate backgrounds were summed and scaled to the size of the object region being measured. Specifically, we used the following regions as background at 70 μm: For positions O1 and O2 in Figure 7a-c, background regions B1 and B5 were averaged and used. For positions O3 and O5, background regions B2 and B4 were used. And for position O4, background regions B2 and B3 were used. At 24 μm we simply used regions B1, B2 and B4, which do not overlap SNR emission.

The signal in each sampled region was measured using the `FUNtools` package that interfaces with `ds9`. [3] As with the total flux estimates, it is necessary to multiply the total signal above background measured in a region by the pixel scale (sr pixel^{-1}). Thus, ratios use the same spatial object regions, even though the pixel sizes varied. The region fluxes and ratios between 24 and 70 μm are provided in Table 2. Only small differences are obtained. In particular, the similarity in ratio between O1 and O3, or O1 and the difference between O2-O1, indicates that there is no significant difference in 70/24 μm ratio between bright radiative and nonradiative regions. This is in keeping with the earlier discussion about the IRS and SED spectra, where these emissions are dominated by the main blast wave.

---

[1] AIPS is produced and supported by the National Radio Astronomy Observatory, operated by Associated Universities, Inc., under contract with the National Science Foundation.

[2] See `http://hea-www.harvard.edu/RD/ds9/` .

[3] `http://hea-www.harvard.edu/RD/funtools/help.html` .

We have also derived ratios of regions between 8 μm and 24 μm using a similar technique, although for somewhat modified spatial regions than used with the 70/24 μm ratios. The defined 8 and 24 μm regions are shown in Figure 7d-f, and details are given at the bottom of Table 1. This comparison is complicated by the faintness of the 8 μm emission, by the presence of many more stars at 8 μm, and by the difference in resolution between the images. Because of potential contamination of the 8 μm image by the [Ar II] 7.0 μm line seen by Roellig & Onaka (2004), the derived ratios may be skewed toward slightly higher 8/24 μm ratios than true. On the other hand, any relative changes in the ratio should be real.

For the 8 μm to 24 μm comparison, positions O1 and O2 isolate the two brightest regions of radiative optical filaments in the NW. Position O3 samples the so-called 'bump' region, which includes both radiative and nonradiative optical emission in the NNW. O4 provides the cleanest sampling of nonradiative shock emission on the northern rim. O5 and O6 sample two regions of central emission knots, but are smaller regions than measured above for the 70/24 μm ratio. Again, optical data suggests a mixture of radiative and nonradiative shocks in these regions. Stars have largely been avoided, with the exception of position O6, for which it was impossible to totally exclude stars from the selected region. At 8 and 24 μm, we simply averaged all three of the background regions shown and applied this as representative to all positions.

We have applied recommended photometric corrections for diffuse sources appropriate for the 8 μm band, as described in the IRAC section of the SSC website[4]. This correction for sources large compared to the calibration aperture for point sources (12″) is a factor of 0.74, which has been applied to measured fluxes and backgrounds for this band. However, this correction is sufficiently poorly known that an additional uncertainty of order 10% is introduced. Any relative changes in the 8/24 μm ratio should remain valid, however.

The derived 8/24 μm ratios are summarized in Table 3. Comparing the measurements at positions O1 and O2 to O4, we see higher ratios at the strongly radiative positions, indicative of contamination of the 8 μm image by line emission (likely [Ar II], as indicated in the IRS spectrum discussion above). Hence, the O4 measurement likely represents the most accurate assessment of the 8/24 μm dust continuum. It is unclear without IRS data whether the higher ratios observed at O3, O5, and O6 are due to variations in the dust continuum or due to significant IR line emission from the optically faint radiative filaments in these regions.

We have not color-corrected the observed fluxes reported in the Tables. Our model fluxes have been produced by integration of the calculated spectrum over the *Spitzer* bandpasses at 24 and 70 μm. Since *Spitzer* fluxes are calibrated by comparison with stars whose spectra

[4]See `http://scc.spitzer.caltech.edu/irac/` .

at 24 μm and longward are well-approximated by the Rayleigh-Jeans limit of a blackbody, we have assumed a λ^{-2} spectrum and calculated what *Spitzer* would report for the flux at the nominal frequency for each band. That is, we have converted our model fluxes into "*Spitzer* space" before computing model ratios, rather than color-correcting observed fluxes. However, such corrections would not be large in any case. Our shock models that reproduce the observed flux ratios give grain temperatures between 75 and 95 K. While the spectra are not exact blackbodies, color corrections for a 70 K blackbody are less than 10% at both 24 and 70 μm, as reported in the MIPS Data Handbook (v3.0, p. 29); at 100 K, they are less than 7% at both wavelengths. For IRAC, color corrections are reported in the IRAC Data Handbook only down to blackbody temperatures of 200 K. For that temperature, corrections are less than 20% for both Channels 3 and 4. We believe that overall calibration errors, estimated in the *Spitzer* Observing Manual, Sec. 8.3.3 (p. 355) to be 10% for extended sources at 24 μm and 15–20% at 70μm, will dominate the errors at those bands. We can also estimate internal statistical errors from the pixel-to-pixel dispersion in the background; these errors are negligibly small compared to those due to calibration. We adopt conservative overall error estimates of 10% at 24 μm and 20% at 70 μm.

In addition to deriving region ratios as described above, we also created a ratio map from the convolved 24 μm image and the 70 μm image as follows. First, we measured a mean background from most of the region on the image not occupied by the source (avoiding obvious point sources), and subtracted that value, at each wavelength. Then we blanked the convolved 24 μm image below 10 MJy/sr, a level corresponding to about 20% of peak, which left all obvious structure intact. (The off-source rms fluctuation level was 0.6 MJy/sr.) At 70 μm, a much noisier image, the off-source rms was about 1.6 MJy/sr; we blanked below 5 MJy/sr, about three times this value. The point of the blanking is to make sure that only pixels whose measured fluxes are highly significant at both wavelengths are used to compute ratios. We then generated the ratio image shown in Fig. 8.

Figure 8 shows several features of interest. First, a general anticorrelation of ratio with 24 μm brightness indicates that hotter (lower 70/24 μm ratio) regions are brighter. Second, the minima in the ratio are actually offset from the 24 μm brightness peaks slightly. Third, the western region of bright radiative shocks appears to have somewhat different ratio. The range of pixels in the image is about 0.3 – 0.8, with a broad maximum around 0.45 and most pixels between 0.35 and 0.5, consistent with the values measured in regions shown in Table 2. Higher ratios in the fainter regions is the primary reason the total 70/24 μm = 0.52 even though most of the brighter regions have lower ratios.

3.3. Grain Emission Modeling

The morphological comparisons across different wavelengths show a clear correlation between the soft X-ray images and IR images at all three MIPS wavelengths, 8, 24 and 70 μm. We thus attribute emission from Kepler in these bands to shocked interstellar and circumstellar dust, heated by the hot, X-ray emitting plasma in the primary blast wave (Dwek & Arendt 1992). Collisions with energetic electrons and ions heat dust grains to $\sim 100K$, where they emit thermal radiation visible to *Spitzer's* mid-IR instruments. In addition to heating, the ions in the plasma sputter dust grains, rearranging the grain-size distribution by destroying small grains and sputtering material off of large grains. We employ computer models of collisionally heated dust to explain what is seen in Kepler, identical to what was done for Type Ia SNRs (Borkowski et al. 2006) and core-collapse SNRs (B. Williams et al. 2006) for SNRs in the Large Magellanic Cloud. Our models use as input an arbitrary grain-size distribution, grain type (astronomical silicates, carbonaceous, etc.), proton and electron density n_p and n_e, ion and electron temperature T_i and T_e, and shock age (or sputtering time scale) $\tau_p = \int_0^t n_p dt$. The model is based on the code described by Borkowski et al. (1994) in the context of photon-heated dust in planetary nebula Abell 30, and augmented to allow for heating by energetic particles in hot plasmas.

Because little is known about the surroundings of Kepler, we adopt a power-law grain size distribution with index α = -3.5 and an exponential cutoff. We use a range of 100 grain sizes from 1 nm to 0.5 μm. We also use only astronomical silicates. This is consistent with past efforts to model dust emission from Kepler (Douvion et al. 2001). We use bulk optical constants for astronomical silicates from Draine & Lee (1984). Energy deposition rates for electrons and protons were calculated according to Dwek (1987) and Dwek & Smith (1996). Because small grains are stochastically heated and have large temperature fluctuations as a function of time, we must account for the increased radiation produced by such transient heating. We use the method described by Guhathakurta & Draine (1989) for this purpose.

It is also necessary to model sputtering for all grains, since sputtering alters the grain size distribution downstream of the shock. Sputtering rates for grains in a hot plasma are taken from Bianchi et al. (2005). Small grains can actually experience an enhancement in sputtering due to the ion knocking off atoms not only from the front of the grain, but also from the sides or the back. We have included such enhancements in our models, with enhanced sputtering yields described by Jurac et al. (1998). Sputtering is very important in the dense CSM environment of Kepler, and results in the efficient destruction of small grains in the postshock gas and very significant modification of the preshock grain size distribution. Even MIPS fluxes and their ratios depend on the shock sputtering age, but because emission in these bands is mostly produced by relatively large grains with moderate

temperature fluctuations, sputtering effects are less extreme than at shorter wavelengths. We consider our dust models reliable for modeling MIPS fluxes and their ratios. Thermal fluctuations are particularly important in very small grains, which reradiate their energy at short wavelengths, so sputtering dramatically reduces the amount of radiation in the IRAC bands.

Contrary to expectations, the 8 μm emission is much stronger than predicted by our models. While we do not include PAHs in our modeling code, they are not likely to be present in large quantities given the absence of their distinctive spectral features in IRS spectra (Roellig & Onaka 2004). However, the model does not account for several physical effects likely to be important for very small grains, such as discrete heating (i.e., discrete energy losses as an electron or proton traverses a grain), and corrections to heating and sputtering rates required when particle mean free paths are much greater than grain radius. For these reasons, we have not attempted to model the 8/24 μm flux ratios shown in Table 3. A great deal of theoretical work remains to be done before the wealth of data produced by *Spitzer* can be used effectively to understand the properties of small grains.

For modeling an outward moving shock wave, we have used a one-dimensional plane-shock approximation. The plane-shock model assumes a constant temperature, but superimposes regions of varying sputtering timescale from zero up to a specified shock age (Dwek et al. 1996). The shock model effectively varies the product of density and time behind the shock, allowing us to account for material that has just been shocked and material that was shocked long ago, since these will experience different amounts of sputtering. The output of our models is a single spectrum, which is produced by superimposing spectra of many different grain sizes. Since we do not model observed spectra directly, we can only fit flux ratios from photometric measurements. We focus here on reproducing the observed 70/24 μm ratios.

We constructed a grid of dust models to explore the parameter spaces of temperature and density, covering electron temperatures kT_e from 0.03 to 10 keV and electron densities n_e ranging from 3 to 10^3 cm^{-3}. We assumed that ion and electron temperatures are equal. The output of the grid was $\sim$ 300 separate models with varying n, T, and τ_p, the shock sputtering age. (Since τ_p inherently contains n_p, and n_p is related by a constant factor to n_e, τ_p is varied from model to model. See Borkowski et al. 2006.) We divide the actual age of Kepler by 3 to approximate an "effective shock age" for Kepler, which was used in the models. The factor of 1/3 arises from applying results of a spherical blast wave model to the plane-shock calculation (Borkowski et al. 2001).

For each of the 300 models, a 70/24 μm ratio was calculated from the output spectrum, and the value of the ratio was plotted on a two-dimensional color-coded plot as a function

of electron density and pressure (see Figure 9). We then added contours to the plot which correspond to measured values of the 70/24 μm ratio from the MIPS images. The three contours are the highest and lowest measured region values (regions O3 and O5, 0.40 and 0.30, respectively; see Table 2), and the value of 0.52 appropriate for the spatially-integrated fluxes. The plasma conditions for the nonradiative regions of Kepler's SNR can be contained for the most part between these contours. Our nonradiative shock models are not applicable at high densities and low temperatures (toward the lower right corner of Fig. 9) because of the onset of radiative cooling. Shocks with an age of 400 yr and solar abundances. for instance, become radiative to the right of the line shown in the lower right corner of Figure 9. We used postshock cooling ages tabulated by Hartigan et al. (1987) to draw this line in the electron temperature–pressure plane.

At low densities (near the left boundary of Fig. 9), our models with equal ion and electron temperatures overestimate the 70/24 μm flux ratio. In this region of plasma parameters, shocks are fast and ion temperatures are generally larger than electron temperatures. Heating of grains by ions becomes relatively more important, resulting in increased grain temperatures and lower 70/24 μm flux ratios relative to shocks with equal ion and electron temperatures. We estimated an electron temperature for the northwest portion of the remnant, where Sankrit et al. (2005) determined a shock speed of 1660 km s^{-1}. We used a simple model for the ion-electron equilibration through Coulomb collisions behind the shock. From this we derived a T_e of 1.2 keV (in the absence of significant collisionless electron heating and assuming a shock age of $\sim$ 150 yr). A shock model with a postshock electron density of 22 cm^{-3} reproduces the measured ratio of 0.40; we mark its position by a star in Figure 9. (Without sputtering, this ratio would have been equal to 0.31.) A noticeable displacement of this model from the middle contour is caused by additional heating by ions in the more sophisticated model with unequal ion and electron temperatures used for the Balmer-dominated shock in the north. Grain temperatures in this model vary from 75 K to 95 K.

Our estimate of a typical electron density in dust-emitting regions of $n_e \sim 20$ cm^{-3} is in reasonable agreement with other estimates, such as the estimate of $7 - 12$ cm^{-3} in the central optical knots (Blair et al. 1991). It should characterize the bulk of the shocked CSM around Kepler, although higher postshock electron densities and lower temperatures (and hence lower shock speeds) are also possible because contours of constant 70/24 μm ratio approximately coincide with lines of constant pressure on the right hand side of Figure 9. While nonradiative Balmer-dominated shocks with speeds less than 1660 km s^{-1} have not been measured to date in Kepler, the highly inhomogeneous optical and X-ray morphologies suggest that plasma conditions in the shocked CSM may vary greatly with position within the remnant. It is likely that shocks are present with velocities less than seen in the Balmer-

dominated shocks but more than seen in radiative shocks. Shocks with such intermediate velocities are best studied at X-ray wavelengths, and a future analysis of the CSM in Kepler based on a new long *Chandra* observation is in progress (Reynolds et al. 2006). It is also likely that fast nonradiative shocks in the south and east travel through gas with densities much less than 20 cm^{-3}; the current MIPS 70 μm data and optical observations are not sensitive enough to study these shocks in much detail.

Our derived value of $n_e T_e = 3 \times 10^8$ cm^{-3} K ($n_e k T_e = 26$ cm^{-3} keV) is in the pressure range considered by Douvion et al. (2001). However, based on the morphological resemblance between the 24 μm image and the nonradiative optical emission, a lower density and higher temperature better characterize the typical dust emitting regions.

3.4. Total Dust Mass and Dust/Gas Ratio

The spatially-integrated IR spectrum of Kepler is produced by grains of widely varying sizes immersed in inhomogeneous plasmas. This results in a wide range of grain temperatures, making determination of a total dust mass model dependent because of the extreme sensitivity of the radiated IR power to the grain temperature. In Appendix A, we estimate the shocked CSM X-ray emission measure in Kepler using a simple plane shock model with a mean temperature of 5 keV and ionization age of 10^{11} cm^{-3} s, without any collisionless heating at the shock front but allowing for energy transfer from ions to electrons through Coulomb collisions. Emission measure-averaged ion and electron temperatures are 8.9 keV and 1.4 keV in this shock model. The only remaining free parameters in the model are a postshock electron density n_e and a total dust mass. We obtain $n_e = 13$ cm^{-3} by matching the measured spatially-integrated 70/24 μm flux ratio of 0.52. (There is a nonnegligible contribution to grain heating from hot ions in this fast shock; as can be inferred from Figure 9, simpler shock models with equal ion and electron temperature of 1.4 keV predict a slighty higher 70/24 μm ratio of 0.58.) We then derive a total dust mass of 5.4×10^{-4} $M_\odot$ from the measured spatially-integrated MIPS fluxes.

We obtain nearly the same mass when we use instead plasma conditions assumed by Douvion et al. (2001), $n_e = 6000$ cm^{-3} and $kT_e = 0.0043$ keV, corresponding to a model spectrum shown by a solid line in their Figure 3, and based on fits to IRAS and ISO observations. (Douvion et al. 2001 quote a smaller dust mass of $1 - 2 \times 10^{-4}$ $M_\odot$, appropriate for their simple model with hot silicate dust at temperature of 107.5 K, significantly hotter than dust in our models.) This agreement between two different mass determinations based on independent data and very different assumed plasma conditions is encouraging; a future more detailed spatially-resolved joint study of *Spitzer* and *Chandra* data should provide us

with a refined dust mass determination. The mass of 5.4×10^{-4} $M_\odot$ refers to dust currently present in the shocked CSM. Most (78%) of dust was destroyed in our fast shock model, implying an initial (preshock) dust mass of 0.0024 $M_\odot$. Because dust destruction rates depend sensitively on the assumed shock speed and its age, our current estimate of the preshock dust mass is rather uncertain.

The total IR flux in the plane shock model discussed above is 1.4×10^{-9} ergs s^{-1} cm^{-2}, in good agreement with IRAS-based fluxes of 1.3×10^{-9} ergs s^{-1} cm^{-2} and 1.6×10^{-9} ergs s^{-1} cm^{-2} listed by Dwek (1987) and Arendt (1989), respectively. The IR luminosity is 2.8×10^{36} ergs s^{-1}. Kepler is a low-luminosity object when compared with SNRs for which this type of analysis has been done with IRAS (e.g., Saken et al. 1992). More recently, Borkowski et al. (2006) derived total luminosities for two of the four SNRs from Type Ia SNe in their study, and B. Williams et al. (2006) derived luminosities for all four of their sample of SNRs from core-collapse SNe in the Large Magellanic Cloud. Of these six remnants, only SNR 0548-70.4 has a luminosity lower than Kepler, and even it is comparable at 2×10^{36} ergs s^{-1}. This SNR is, however, several times larger (and thus likely older) than Kepler. Indeed, most of the remnants in these two studies have luminosities much higher than Kepler.

A specific object of interest for comparison is Tycho, a Type Ia SNR of comparable age located at a 2 kpc distance. The IR flux of Tycho is 5×10^{-9} ergs cm^{-2} s^{-1} (Arendt 1989), so its IR luminosity is comparable to Kepler. Dust in Tycho is much cooler than in Kepler (Arendt 1989, Saken et al. 1992), consistent with a much lower ISM density around Tycho. SNR 0509-67.5, one of the remnants studied by Borkowski et al. (2006) in the LMC, appears very similar to Tycho. While observations of light echoes (Rest et al. 2005) have placed the age of this SNR at $\sim$ 400 yr, a high shock speed deduced from optical and UV observations of Balmer-dominated shocks (Ghavamian et al. 2007) implies a low ambient ISM density. Its MIPS 24 μm flux is 16.7 mJy, about 2–4 times lower than what Tycho or Kepler would have at a distance of 50 kpc. An upper limit to its dust mass is 0.0011 $M_\odot$, and SNR 0509-67.5 is likely less luminous in the IR than Tycho or Kepler.

Determination of the dust/gas mass ratio requires knowledge of the shocked CSM gas mass. Using an X-ray emission measure of 10 $M_\odot$ cm^{-3} (Appendix A) and $n_e = 13$ cm^{-3}, we derive a total shocked CSM mass in Kepler of 0.77 $M_\odot$. This is in good agreement with a shocked CSM mass of 0.95 $M_\odot$ derived from *ASCA* observations (Kinugasa & Tsunemi 1999), after scaling their results to the 4 kpc distance used here and using an electron density of 13 cm^{-3}. The hydrodynamical model of Borkowski et al. (1992, 1994), based on the massive core-collapse runaway progenitor scenario of Bandiera (1987), requires ~ 1 $M_\odot$, also in reasonable agreement with the present mass estimate. Recent hydrodynamical models of Velázquez et al. (2006), based on a Type Ia progenitor scenario, require several $M_\odot$ of

shocked CSM. But Velázquez et al. (2006) used collisional equilibrium ionization X-ray spectral models, which underestimate X-ray emission by an order of magnitude or more for young SNRs (Hamilton et al. 1983; see also Appendix A), resulting in an excessive estimate of the shocked mass by a comparable factor.

Combined with the dust mass from above of 0.0024 $M_{\odot}$, we arrive at a dust-to-gas mass ratio for the CSM surrounding Kepler of 0.003. This is lower than the generally accepted figure for the Galaxy (e.g., Weingartner & Draine 2001) by a factor of several. Since the dust in Kepler appears to have originated in some kind of a stellar outflow, the lower dust content may be related to this and not a characteristic of the general ISM in the region. Kepler's dust/gas ratio is higher by a factor of several than found for SNRs in the Magellanic Clouds (Borkowski et al. 2006; B. Williams et al. 2006; Bouchet et al. 2006), most likely because of the high (near or above solar) metallicity of its SN progenitor compared with the ∼0.4 solar LMC abundance.

3.5. North-South Density Gradient

A number of indicators imply a potential difference in preshock density from north to south across the Kepler region. The difference in the surface brightness of the north rim compared to the south rim is one indicator, and the effect may be visible directly from the background in Fig. 1 and the appearance of the 160 μm image in Fig. 2e. The south rim is only faintly visible at 24 μm, while the north rim is extremely bright. We believe the 24 μm is dominated by dust emission, although some contribution from emission lines cannot be ruled out without spectra. Under this assumption, we took a small region of the southern rim and an equal-sized region of the northern rim that is dominated by nonradiative shocks and measured the flux from both regions at 24 μm. The regions were arcs following the shape of the rim, approximately 23″ in thickness and 75″ in length. The south region follows the faint southern rim at a declination of approximately -21:31:04 (J2000). We found a north/south ratio of 24 μm fluxes of ∼30. A possible explanation for this contrast is that the shocks are encountering regions of different density.

We have made several estimates of the density contrast necessary to produce the observed intensity ratio. First, we assume that the dust-to-gas mass ratio in the two regions is the same (although we make no *a priori* assumptions about what that ratio must be). We do not assume equal amounts of swept-up material in the two regions, but rather simply vary the gas density (and dust mass accordingly) in the models and assume the same shock speed (and thus the same temperature) for both regions. This method reproduces the observed flux difference with a modest density contrast of only a factor of ∼4.5. It should be noted

that these are all post-shock densities.

As an alternative approach to this problem, one can relax the requirement that the shock speeds be equivalent in the two regions, since a variation in density should cause variations in shock speed. We repeated the calculations for several different shock speeds in the south region, while keeping the north region constant at 1660 km s^{-1}, and a density of $n_e = 19.5$ cm^{-3}. We calculated electron and proton temperatures for the south region with these different shock speeds assuming no equilibration at the shock front, and used these different temperatures to predict dust emission at 24 μm. In these models, the density contrast required is only weakly dependent on shock speed. While grains are heated to hotter temperatures in faster shocks, the amount of destruction of grains also increases. Overall, we find that for a reasonable range of shock speeds up to 3000 km s^{-1}, a post-shock density contrast between 4 and 7 times lower in the south (and accordingly 4–7 times less dust present) can reproduce the observed ratio. The density contrast increases with faster shock speeds.

As a third approach, we consider the remnant to be in pressure equilibrium. Keeping the density and shock speed in the northern region constant with the values mentioned above, we varied the shock speed in the south and derived density from the pressure equilibrium expression $n_N V_N^2 \equiv n_S V_S^2$, where subscripts N and S refer to the north and south regions, respectively. Under this constraint, we determined the shock speed required to reproduce the observed 24 μm flux ratio, again assuming a constant dust-to-gas mass ratio. We find that a shock with speed $\sim$5000 km s^{-1}, and thus a density of ~ 2.1 cm^{-3} can account for the difference in fluxes coming from the two regions. This is a density contrast of 9.1. Because 5000 km s^{-1} is much higher than inferred from other indicators, this contrast in density is considered an upper limit. The predicted 70/24 μm flux ratio in the south region is ~ 1.2, which is significantly higher than in the brighter regions of the remnant, but consistent with the idea that the dust in that region is cooler. It is also consistent in a general sense with the higher overall average 70/24 μm ratio of 0.52. Since the these models are only constrained by the fluxes observed at 24 μm in the south, these results should be considered tentative. Detailed mid-infrared spectroscopy will be required to investigate this issue further.

3.6. Whither the Cold Dust Component?

Morgan et al. (2003; hereafter M03) have recently reported excess emission in Kepler using SCUBA 450 and 850 μm observations. They model this as a cold astronomical silicate dust component from ejecta ($T_d = 17$ K), inferring as much as a solar mass of material in this component. Dwek (2004a) proposes a differing interpretation, arguing instead for

a component at $T_d = 8$ K and a much lower mass of dust in the form of Fe needles. He supports the general possibility of a cold dust component related to the ejecta, pointing to a similar component identified in Cas A (Dwek 2004b), but the amount of mass involved would be much lower than inferred by M03. Douvion et al. (1991) would not have been able to detect this cold component.

Our MIPS 160 μm image shown in Figure 3 is directly relevant to this discussion since this wavelength is close to the peak of the cold component curve predicted by M03 (see their Figure 2). No emission related to the SNR shell or interior is detected at 160 μm, although the background is patchy and there appears to be a general gradient of intensity from NE toward the SW in the image.

To derive an upper limit at 160 μm, we extracted emission from the region corresponding to the SNR location (judging from an aligned overlay of the 24μm image) and from nearby background regions, as described above for the 24 and 70 μm images. Background levels to the north and east of the SNR are at a higher level than the average from the object location, while the background level in the south is slightly below the object region average. The observed field of view is very close to the western edge of the SNR, but the background in that region appears to be comparable to that in the south. To be conservative, we apply the southern background level to the entire object, which will over-estimate any contribution from the SNR. The resulting upper limit we derive is 0.8 Jy at 160 μm, which is approximately a factor of 10 below the value predicted by M03 from the SCUBA-based model. Hence, our *Spitzer* 160 μm data do not confirm the M03 cold-dust picture. This fairly conservative upper limit does not rule out the idea of Fe needles as discussed by Dwek (2004a), but the presence of any such component in Kepler has been argued against on theoretical grounds (Gomez et al. 2005). Even if present, any such component in Kepler's SNR would contain well below 0.1 solar mass, and would not require a massive precursor star as in the M03 interpretation.

3.7. Synchrotron Emission

X-ray synchrotron emission has been reported for Kepler: thin filaments seen in the eastern "ear" extension (Bamba et al. 2005), broader emission from the SE quadrant (Cassam-Chenaï et al. 2004), and an extension of the integrated flux to hard X-rays (Allen, Gotthelf, & Petre 1999). The X-ray fluxes demand a steepening of the extrapolated radio spectrum; if that steepening occurs at shorter than IR wavelengths, IR synchrotron emission should be present with a morphology identical to the radio and at readily extrapolated brightness levels. While the average radio spectral index of Kepler is –0.71 ($S_\nu \propto \nu^\alpha$) (DeLaney et

al. 2002), higher-frequency archival radio data imply a value of –0.59 (Reynolds & Ellison 1992). This concave-up curvature, or hardening to shorter wavelengths, can occur for electrons accelerated in a shock modified by the pressure of accelerated ions (Ellison & Reynolds 1991). If we extrapolate from images at cm wavelengths (e.g., DeLaney et al. 2002) with this value, we predict surface brightnesses at 3.6 μm in the range 0.6 – 1.1 μJy arcsec^{-2} (or $(2.5-4.8)\times10^{-2}$ MJy sr^{-1}). Our 3.6 μm image shows only a faint hint of any emission associated with Kepler. In particular, there is no apparent emission in the SE quadrant. Typical brightness levels are 0.4 – 0.5 MJy sr^{-1}, or 10 – 20 times the extrapolated synchrotron flux. Even with very significant hardening of the spectrum above 10 GHz, the 3.6 μm data are not constraining the presence of synchrotron emission. In particular, the regions identified by Bamba et al. (2005) and Cassam-Chenaï et al. (2004), the SE quadrant and the eastern "ear," are very faint in IR in general. The western "ear" may also harbor X-ray synchrotron emission, and it too is fainter at 24 μm relative to the rest of the shell emission. Far more sensitive IR observations would be necessary to detect synchrotron emission.

4. Discussion

Of the historical SNe, Kepler's remains enigmatic because a clear determination of the SN type (and thus precursor star) has proven elusive. Claims of evidence supporting both a massive precursor (core collapse SN type) or a white dwarf precursor (Type Ia SN) abound in the literature over the last decade or more. In this section, we discuss this issue and highlight new insights that may help resolve this dichotomy.

Firstly, since not all SN ejecta can form into dust, the claim by M03 of a solar mass or more of cold dust in Kepler was an indication of even more ejecta mass and hence a massive precursor star. The negative detection at 160 μm here points to an apparent problem with the SCUBA result, presumably due to the complex and variable background observed in this region. Hence, a massive precursor is not required by the IR data.

Another indication pointing toward a massive precursor star has been the overabundance of nitrogen in the optically-emitting filaments, which are thought to represent dense knots of CSM being overrun by the blast wave. We have run a small grid of shock models using the current version of the shock code described by Raymond (1979) and Hartigan et al. (1987) for comparison with the optical spectrum of knot 'D3,' a bright, radiative shock knot presented by Blair et al. (1991, their Table 2). We find that the main features of this spectrum can be matched with a model similar to model E100 of Hartigan et al. (1987), but with the N abundance increased by 0.5 dex. This is indeed a significant enhancement over solar abundance.

However, solar abundances are the wrong reference point. At a distance of ∼4 kpc and galactic coordinate G4.5+6.8, Kepler's SNR is nearly half way to the galactic center. Rudolph et al. (2006) provide a summary of galactic abundance gradients, and for nitrogen find an increase of ∼0.3 dex for the assumed distance of Kepler's SNR. Additionally, inspection of their Figure 4 shows that the scatter in observed points around the best fit line for the gradient readily encompasses the required value of 0.5 dex enhancement in nitrogen at Kepler's distance from the galactic center. While the nitrogen abundance around Kepler's SNR may be enhanced relative to its local surroundings, it is not required, and certainly the magnitude of any enhancement is considerably less than has been recognized previously.

We note, however, that this in no way negates the fact that the presence of dense material surrounding Kepler's SN is surprising for an object nearly 500 pc off the galactic plane. This material must have its origin in either the precursor star, or the precursor system (if a binary of some type was involved). Canonical wisdom says that core collapse precursors are massive stars, and massive stars shed material via stellar winds prior to exploding. Type Ia SNe are thought to arise from white dwarf stars that are pushed over the Chandrasekhar limit, although the exact details of the precursor system that gives arise to this are still widely debated (e.g. Livio & Riess 2003, and references therein). The absence of hydrogen lines in the spectra of Type Ia SNe is taken as evidence for CO white dwarfs with little or no photospheric hydrogen, and certainly little if any CSM.

Improved statistics on extragalactic SNe, however, are finding exceptions to this general scenario. A small but growing class of bona fide (confirmed with spectra) Type Ia SNe has been found that show narrow hydrogen lines at late times, indicating the presence of a CSM component close to these objects. SN 2002ic is a recent example of this phenomenon. Some authors dub these objects Type Ia/IIn (e.g., a Type Ia with narrow hydrogen lines; Kotak et al. 2004) while others denote such objects as a new SN type, IIa (i.e., a Type Ia with hydrogen lines; Deng et al. 2004). Whatever the designation, these objects demonstrate that some SNIa explosions can occur in regions with significant CSM, albeit at distances closer in to the SN than inferred for Kepler. Any such close in component near Kepler's SN, if present, would have long since been overrun by the blast wave.

Direct evidence for the presence of (presumably) CSM material around another Type Ia SN was provided by *Hubble* Space Telescope images of light echoes around SN 1998bu (Garnavich et al. 2001; Patat 2005). Among several light echoes detected in this SN, there is an echo generated by scattering off dust located closer that 10 pc to the SN. At the same time, SN 1998bu has one of the most stringent upper limits on the density of the stellar wind (Panagia et al. 2006). The presence of a detached CSM (or perhaps an ISM shell swept-up by winds of the SN progenitor) is likely in this nearby SN. These and similar observations

open up the possibility that Kepler's SNR represents a local example of this phenomenon.

Finally, it should be noted that recent detailed X-ray observations and modeling (Kinugasa & Tsunemi 1999; Cassam-Chenaï et al. 2004) are consistent with Si and Fe-rich ejecta, but show no evidence for other enhancements seen in core collapse SNRs such as Cas A (Hughes et al. 2000; Hwang & Laming 2003). The temperature structure inferred within the X-ray ejecta, with Fe K peaking interior to Fe L is reminscent of Type Ia SNRs such as SN1006 and Tycho (Hwang & Gotthelf 1997; DeCourchelle et al. 2001). These early results are strengthened almost to the point of certainty by a recent deep *Chandra* X-ray exposure on Kepler that will allow a detailed assessment of abundances within the ejecta of Kepler (Reynolds et al. 2006). The preponderance of evidence from the X-rays now points toward a Type Ia origin for the precursor of Kepler's SNR.

If Kepler represents a SNIa explosion in a region with significant CSM, it would be important from two directions: If plausible models are put forward that can explain a Type Ia with significant CSM, applying them to Kepler's SNR may provide a stringent test because of its proximity and wealth of supporting observational data. On the other hand, Kepler is only one object, and observations of additional extragalactic examples of SNIa's with CSM in various forms may provide important clues about the frequency and/or the progenitor population of such explosions (e.g. Mannucci 2005).

5. Conclusions

We have presented *Spitzer* imaging of Kepler's supernova remnant at 3.6, 4.5, 5.8, 8, 24, 70, and 160 μm wavelengths and compared with data from other wave bands. Emission associated with the remnant is obvious at all except 160 μm, but emission in the two shortest-wavelength IRAC bands is visible only at the locations of bright optical radiative shocks in the WNW. However, at 24 μm, the entire periphery of the remnant can be seen, along with emission seen, at least in projection, toward the interior.

To summarize, we find:

- The 24 μm emission is well correlated with the outer blast wave as delineated by soft X-ray emission and by nonradiative (Balmer-dominated) shocks seen in the optical. This is clearly emission from dust heated by collisions in the X-ray emitting material. It is not well correlated either with ejecta emission (shown by strong Fe L-shell emission in X-rays) or with dense regions containing radiative shocks. In particular, we find no evidence for dust newly formed within the ejecta material.

- The emission at 8 μm largely resembles that of the brightest regions at 24 μm, although contamination by line emission in the 8 μm is apparent in the radiative shock regions. This similarity indicates that even short-wavelength emission originates from the same grain population as that at longer wavelengths. However, current models are not yet able to describe emission from the implied population of small grains.

- The emission at 70 μm is similar to that at 24 μm, but a higher background makes it difficult to discern the fainter southern half of the remnant. Where both 70 μm and 24 μm emission can be seen, 70/24 μm flux ratios for discrete regions range from 0.37 to 0.49. Lower values, implying higher temperatures, are correlated with brighter regions. A total object average ratio of 0.52 implies that the fainter regions tend toward higher values of this ratio.

- The SED spectrum indicates that lines make at most a small contribution between 55 and 95 μm. The spectrum, along with the absence of emission at 160 μm, rules out the presence of large amounts of cold dust.

- Dust models using a power-law grain size distribution and including grain heating and sputtering by X-ray emitting gas can explain observed 70/24 μm flux ratios with sensible parameters. The models give gas densities of 10 – 20 cm^{-3}. The range of observed ratios can be explained by ranges of temperature and density of different regions in rough pressure equilibrium.

- We find a total dust mass of about 5.4×10^{-4} $M_{\odot}$ after sputtering, and infer an original mass of about 2.4×10^{-3} $M_{\odot}$. With an estimate of shocked gas mass from X-ray data, we infer an original dust/gas ratio of about 3×10^{-3}, lower by a factor of several than normally assumed for the Galaxy, as has been found for several other supernova remnants.

- We find that a moderate density contrast in the range of $\sim$4 – 9 is required to explain the brightness variations observed between the north and south rims of the remnant at 24 μm, depending somewhat on the assumptions and models applied.

- We suggest the preponderance of current evidence from optical, X-ray, and infrared data and modelling now points toward a Type Ia supernova, albeit in a region of significant surrounding CSM/ISM, especially for an object so far off the galactic plane. A possible similarity to several extragalactic Type Ia supernovas with narrow hydrogen lines at late times is pointed out.

Data from the *Spitzer Space Telescope* clearly demand more sophisticated grain modeling. The absence of large quantities of newly formed dust challenges models hypothesizing

such dust formation in the SN ejecta. However, the heated dust from the circumstellar medium heated by the blast wave can provide useful diagnostics of plasma conditions.

It is a pleasure to thank the *Spitzer* operations team at JPL for their efforts in obtaining these data. We also thank the public relations staffs at the *Spitzer*, STScI, and *Chandra* operations centers for producing the color image in Figure 6, which was part of a photo release for the 400th anniversary of SN1604 in October 2004. This research has made use of SAOimage `ds9`, developed by the Smithsonian Astrophysical Observatory. This work is supported by JPL grant JPL-1264303 to the Johns Hopkins University.

6. Appendix: X-ray Emission Measure of the Shocked CSM

We have used archival *XMM-Newton* data to estimate the emission measure of the shocked CSM around Kepler's SNR. While Kepler's X-ray spectrum is dominated by ejecta emitting strongly in lines of heavy elements such as Fe, Si, and S, Ballet (2002) noted a good match between an RGS1 image around the O Lyα line and the optical Hα images. This suggests that the low-energy X-ray emission dominated by N and O originates in the shocked CSM. The Lyα lines of N and O, and the Heα line complex of O, are well separated from strong Fe L-shell lines in the RGS spectra (see Figs. 1 and 2 in Ballet 2002). We used these spectra to arrive at the following N and O line fluxes: 2.5×10^{-13} ergs cm^{-2} s^{-1} for N VII λ24.779, 7.5×10^{-13} ergs cm^{-2} s^{-1} for the O VII Heα complex at $\sim$ 21.7 Å, and 2.8×10^{-12} ergs cm^{-2} s^{-1} for O VIII λ18.967. The measured O VIII λ18.967 flux may include a non-negligible contribution from O VII Heβ λ18.627, as these two lines blend together in the RGS spectra.

We have used a nonequilibrium-ionization (NEI) thermal plane-parallel shock without any collisionless heating at the shock front to model N and O line fluxes. This plane shock model is available in XSPEC as `vnpshock` model (Arnaud 1996; Borkowski et al. 2001). We assumed that N and O lines are produced in fast (2000-2500 km s^{-1}; Sollerman et al. 2003) nonradiative, Balmer-dominated shocks with a mean post-shock temperature of $\sim$ 5 keV. The ISM extinction $E(B-V)$ toward Kepler is equal to 0.90 (Blair et al. 1991), and with $R_V = A_V/E(B-V) = 3.1$ and $N_H = 1.79 \times 10^{21} A_V$ cm^{-2} (Predehl & Schmitt 1995), N_H is equal to 5.0×10^{21} cm^{-2}. We assumed solar abundances for O (from Wilms et al. 2000). We can reproduce O VII Heα and O VIII λ18.967 (+ O VII Heβ λ18.627) fluxes with an emission measure $EM = n_e M_g$ equal to $10 M_\odot$ cm^{-3} (at the assumed 4 kpc distance) and a shock ionization age of 10^{11} cm^{-3} s. By matching the measured N VII λ24.779 flux, we arrive at an oversolar (1.6) N abundance, confirming again the nitrogen overabundance in

the CSM around Kepler.

The shock ionization age cannot be estimated reliably based on the measured N and O line fluxes alone. These lines are produced close to the shock front, and their strengths depend only weakly on the shock age. Shocks with different ages can satisfactorily reproduce the observed O and N line fluxes, with the emission measure EM inversely proportional to the shock age in the relevant shock age range from 5×10^{10} cm^{-3} s to 4×10^{11} cm^{-3} s. Additional information is necessary to constrain the shock ionization age, such as fluxes of Ne and Mg lines or the strength of the continuum at high energies. Because the X-ray spectrum of Kepler is dominated by ejecta at higher energies, it is very difficult to separate CSM emission from the ejecta emission in the spatially-integrated *XMM-Newton* spectra. We note, however, that shocks with ages of 2×10^{11} cm^{-3} s and longer produce more emission than seen in Kepler. In particular, the Mg lines and the high energy continuum are too strong. For ionization ages as short as 5×10^{10} cm^{-3} s, the O Heα/O Lyα line ratio becomes excessive (0.36) in the model versus observations (0.28). Such short ionization ages may still be plausible if shock ages are as short as ~ 80 yr and postshock electron densities are ~ 20 cm^{-3} as implied by infrared data.

We conclude that a reasonable estimate of the CSM emission measure, equal to $10 M_{\odot}$ cm^{-3}, is provided by a plane shock with an age of 10^{11} cm^{-3} s. However, the EM is known only within a factor of 2 because of the poorly known shock ionization age and uncertain (perhaps spatially varying) absorption. (A 10% range in absorption listed by Blair et al. (1991) results in 35–40% error in the derived EM.) It is also possible, even likely, that X-ray emission is produced in a variety of shocks with different speeds driven into gas with different densities. In this case, low energy X-ray emission would be predominantly produced in slow shocks, while high energy emission would originate in fast shocks. A single shock approximation used here might then underestimate the true CSM emission measure. A future X-ray study based on available high spatial-resolution *Chandra* data will help in resolving such issues, and will result in better estimates of the CSM emission measure.

REFERENCES

Allen, G., Gotthelf, E., & Petre, R. 1999, Proc. 26th ICRC, 3, 480

Arendt, R. G. 1989, ApJS, 70, 181

Arendt, R. G., Dwek, E., & Moseley, S. H. 1999, ApJ, 521, 234

Arnaud, K. A. 1996, in Astronomical Data Analysis and Systems V, eds. G.Jacoby & J.Barnes, ASP Conf. Series, v.101, 17

Baade, W. 1943, ApJ, 97, 119

Ballet, J. 2002, in High Resolution X-ray Spectroscopy with *XMM-Newton* and *Chandra* (London)

Bamba, A., Yamazaki, R., Yoshida, T., Terasawa, T., & Koyama, K. 2005, ApJ, 621, 793

Bandiera, R. 1987, ApJ, 319, 885

Bianchi, L., et al. 2005, ApJ, 619, 71

Blair, W. P. 2005, in "1604-2004: Supernovae as Cosmological Lighthouses," ASP Conf. Ser. 342, ed. by M. Turatto, S. Benetti, L. Zampieri, & W. Shea (San Francisco: ASP) 416

Blair, W. P., Long, K. S., & Vancura, O. 1991, ApJ, 366, 484

Borkowski, K. J., Blondin, J. M., & Sarazin, C. L. 1992, ApJ, 400, 222

Borkowski, K. J., Harrington, J. P., Blair, W. P., & Bregman, J. P. 1994, ApJ, 435, 722

Borkowski, K. J., Lyerly, W. J., & Reynolds, S. P. 2001, ApJ, 548, 820

Borkowski, K. J., et al. 2006, ApJ, 642, L141

Borkowski, K. J., Sarazin, C. L., & Blondin, J. M. 1994, ApJ, 429, 710

Bouchet, P., De Buizer, J. M., Suntzeff, N. B., Danziger, I. J., Hayward, T. L., Telesco, C. M., & Packham, C. 2004, ApJ, 611, 394

Cassam-Chenaï, G., et al. 2004, A&A, 414, 545

Decourchelle, A., & Ballet, J. 1994, A&A, 287, 206

Decourchelle, A., et al. 2001, A&A, 365, L218

DeLaney, T., et al. 2002, ApJ, 580, 914

Deng, J., Kawabata, K. S., Ohyama, Y., Nomoto, K., Mazall, P. A., Wang, L., Jeffery, D. J., Iye, M., Tomita, H., & Yoshii, Y. 2004, ApJ, 605, L37

Doggett, J. B., & Branch, D. 1985, AJ, 90, 2303

Douvion, T., LeGage, P. O., Cesarsky, C. J., & Dwek, E. 2001, A&A, 373, 281

Draine, B. T., & Lee, H. M. 1984, ApJ, 258, 89

Dunne, L. et al. 2003, Nature, 424, 285

Dwek, E. 1987, ApJ, 322, 812

Dwek, E. 2004a, ApJ, 607, 848

Dwek, E. 2004b, ApJ, 611, 109

Dwek, E., & Arendt, R. G. 1992, ARA&A, 30, 11

Dwek, E., Foster, S. M., & Vancura, O. 1996, ApJ, 457, 244

Dwek, E., & Smith, R. K. 1996, ApJ, 459, 686

Ellison, D. C., & Reynolds, S. P. 1991, ApJ, 382, 242

Elmhamdi, A., et al. 2003, MNRAS, 338, 939

Fazio, G. G., et al. 2004, ApJS, 154, 10

Garnavich, P., et al. 2001, BAAS, 33, 1370

Gerardy, C. L., & Fesen, R. A. 2001, AJ, 121, 2781

Ghavamian, P., Blair, W. P., Sankrit, R., Raymond, J. C., & Hughes, J. P. 2007, ApJ, submitted

Gomez, H. L., Dunne, L., Eales, S. A., Gomez, E. L., & Edmunds, M. G 2005, MNRAS, 361, 1021

Guhathakurta, P. & Draine, B. T. 1989, ApJ, 345, 230

Hamilton, A. J. S., Chevalier, R. A., & Sarazin, C. L. 1983, ApJS, 51, 115

Hartigan, P., Raymond, J., & Hartmann, L. 1987, ApJ, 316, 323

Hughes, J. P. 1999, ApJ, 527, 298

Hughes, J. P., Rakowski, C. E., Burrows, D. N., & Slane. P. O. 2000, ApJ, 528, L109

Hwang, U. & Gotthelf, E. V. 1997, ApJ, 475, 665

Hwang, U. & Laming, J. M. 2003, ApJ, 597, 362

Jurac, S., Johnson, R. E., & Donn, B. 1998, ApJ, 503, 247

Kepler, J. 1606, De Stella Nova

Kinugasa, K., & Tsunemi, H. 1999, PASJ, 51, 239

Kinugasa, K., & Tsunemi, H. 2000, Adv. Sp. Res., 25, 559

Kotak, R., Meikle, W. P. S., Adamson, A., & Leggett, S. K. 2004, MNRAS, 354, L13

Krause, O., Birkman, S. M., Rieke, G. H., Lemke, D., Klass, U., Hines, D. C., & Gordon, K. D. 2004, Nature, 432, 596

Livio, M., & Riess, A. G. 2003, ApJ, 594, L93

Mannucci, F. 2005, in "1604-2004: Supernovae as Cosmological Lighthouses," ASP Conf. Ser. 342, ed. by M. Turatto, S. Benetti, L. Zampieri, & W. Shea (San Francisco, ASP), 140

McCray, R. 1993, ARAA, 31, 175

Morgan, H. L., Dunne, L., Eales, S. A., Ivison, R. J., & Edmunds, M. G. 2003, ApJ, 597, L33

Panagia, N., Van Dyk, S. D., Weiler, K. W., Sramek, R. A., Stockdale, C. J., & Murata, K. P. 2006, ApJ, 646, 369

Patat, F. 2005, in "1604-2004: Supernovae as Cosmological Lighthouses," ASP Conf. Ser. 342, ed. by M. Turatto, S. Benetti, L. Zampieri, & W. Shea (San Francisco, ASP), 229

Predehl, P., & Schmitt, J. H. M. M. 1995, A&A, 293, 889

Raymond, J. C. 1979, ApJS, 39, 1

Rest, A., et al. 2005, Nature, 438, 1132

Reynolds, S. P., & Ellison, D. C. 1992, ApJ, 399, L75

Reynolds, S. P., et al. 2006, AAS 209, #156.17

Reynoso, E. M., & Goss, W. M. 1999, AJ, 118, 926

Rieke, G. H., et al. 2004, ApJS, 154, 25

Roellig, T. L., & Onaka, T. 2004, BAAS, 36, 1520

Rudolph, A. L., Fich, M., Bell, G. R., Norsen, T., Simpson, J. P., Haas, M. R., & Erickson, E. F. 2006, ApJS, 162, 346

Saken, J. M., Fesen, R. A., & Shull, J. M. 1992, ApJS, 81, 715

Sankrit, R. Blair, W. P., DeLaney, T., Rudnick., L., Harrus, I. M., & Ennis, J. A. 2005, Adv. Sp. Res., 35, 1027

Schaefer, B. E. 1996, ApJ, 459, 438

Sollerman, J., Ghavamian, P., Lundqvist, P., & Smith, R. C. 2003, A&A, 407, 249

Velázquez, P. F., Vigh, C. D., Reynoso, E. M., Gómez, D. O., & Schneiter, E. M. 2006, ApJ, 649, 779

Weingartner, J. C., & Draine, B. T. 2001, ApJ, 548, 296

Williams, B. J., et al. 2006, ApJ, 652, L33

Williams, R. M., Chu, Y-H., & Gruendl, R. 2006, AJ, 132, 1877

Wilms, J., Allen, A., & McCray, R. 2000, ApJ, 542, 914

Figure Captions

Fig. 1.— Full field of view MIPS 24 μm image of Kepler's SNR. Scaling is set to a compromise level to show the overall structure to best advantage. The 24 μm image is by far the deepest and most detailed of the *Spitzer* images.

Fig. 2.— A six-panel color figure concentrating on the IRAC images and their comparison to other wavelength bands. Panel a shows a three-color IRAC image with 8 μm in red, 5.6 μm in green and 3.6 μm in blue. Panel b is similar, but for 5.6 μm in red, 4.5 μm in green, and 3.6 μm in blue. The orange color of the SNR filaments indicates emission in both 4.5 and 5.6 μm, but only from the brightest filaments seen at 8 μm. Panel c is a difference image of 8 μm minus 5.6 μm, scaled to show the extent of faint emission at 8 μm. Panel d shows the 4.5 μm minus 3.6 μm difference image. Panel e shows the 24 μm MIPS image from Fig. 1 to the same scale as the other images. The 8 μm image closely tracks the brightest regions at 24 μm. Panel f shows the soft band (0.3 - 0.6 keV) *Chandra* image from archival data, which again looks astonishingly like the 8 μm image in panel c. All images are aligned and scaled exactly the same.

Fig. 3.— A six-panel color figure concentrating on the MIPS images and their comparison to other wavelength bands. Panels a and b show the MIPS 24 μm data with a hard stretch and a soft stretch, respectively, to show the full dynamic range of these data. Panel c shows the MIPS 70 μm data after running through the GeRT software to improve the appearance of the background. Panel e shows the MIPS 160 μm data for the same field of view, although no SNR emission is actually seen at this wavelength. Panel d shows the star-subtracted Hα image from Blair et al. (1991). Panel f shows a three-color representation of the *Chandra* data for Kepler, with the red being 0.3 - 0.6 keV (as in Fig. 2f), green being 0.75 - 1.2 keV, and blue being 1.64 - 2.02 keV.

Fig. 4.— SED apertures selected for assessing the bright NW radiative emission and the sky background, projected on the 24 μm image.

Fig. 5.— Background subtracted SED 55 - 95 μm spectrum of the NW region of Kepler's SNR, as indicated in Figure 4.

Fig. 6.— A color view of Kepler showing data from *Spitzer* 24 μm (red), *Hubble* ACS Hα (yellow), and *Chandra* medium (blue) and soft (green) X-ray emission bands. Despite the differing intrinsic resolutions of the various data sets, they have been carefully coaligned. A

Hubble continuum-band image was used to subtract the stars from this image. See text for details.

Fig. 7.— This figure shows the object and background extraction regions selected for determining ratios between 24 and 70 μm (panels a and b) and between 8 and 24 μm (panels d and e). For reference, the regions are also projected onto the optical Hα image from Blair et al. (1991) in panels c and f. Note that the images shown in panel a and d are the versions that have been convolved to the lower resolution image. Also, panel b shows the original (non-GeRT-corrected) 70 μm image. The labels are used in the text and Tables 2 and 3.

Fig. 8.— A ratio image of the 70 μm and 24 μm data, where only the regions with significant signal have been kept. The color bar provides an indication of the measured ratio, ranging from 0.28 to 0.9. A simple contour from the 24 μm image is shown for comparison. Note the lower values of the ratio in the regions of brightest emission, indicating they are somewhat warmer.

Fig. 9.— The 70/24 μm MIPS flux ratio as a function of electron density and pressure for plane shock dust models discussed in the text. The background color scale indicates 70/24 μm ratio, as indicated by the color bar at right. Dashed lines are lines of constant temperature. The solid magenta diagonal line at lower right indicates where the modeled shocks would become radiative, assuming solar abundance models and an age of 400 years. Three *solid curves* are lines of constant 70/24 MIPS flux ratios, 0.30, 0.40, and 0.52 (from top to bottom), encompassing measured ratios listed in Table 2 and the spatially-integrated ratio. Position of a Balmer-dominated fast (1660 km s^{-1}) shock in the north is marked by a star.

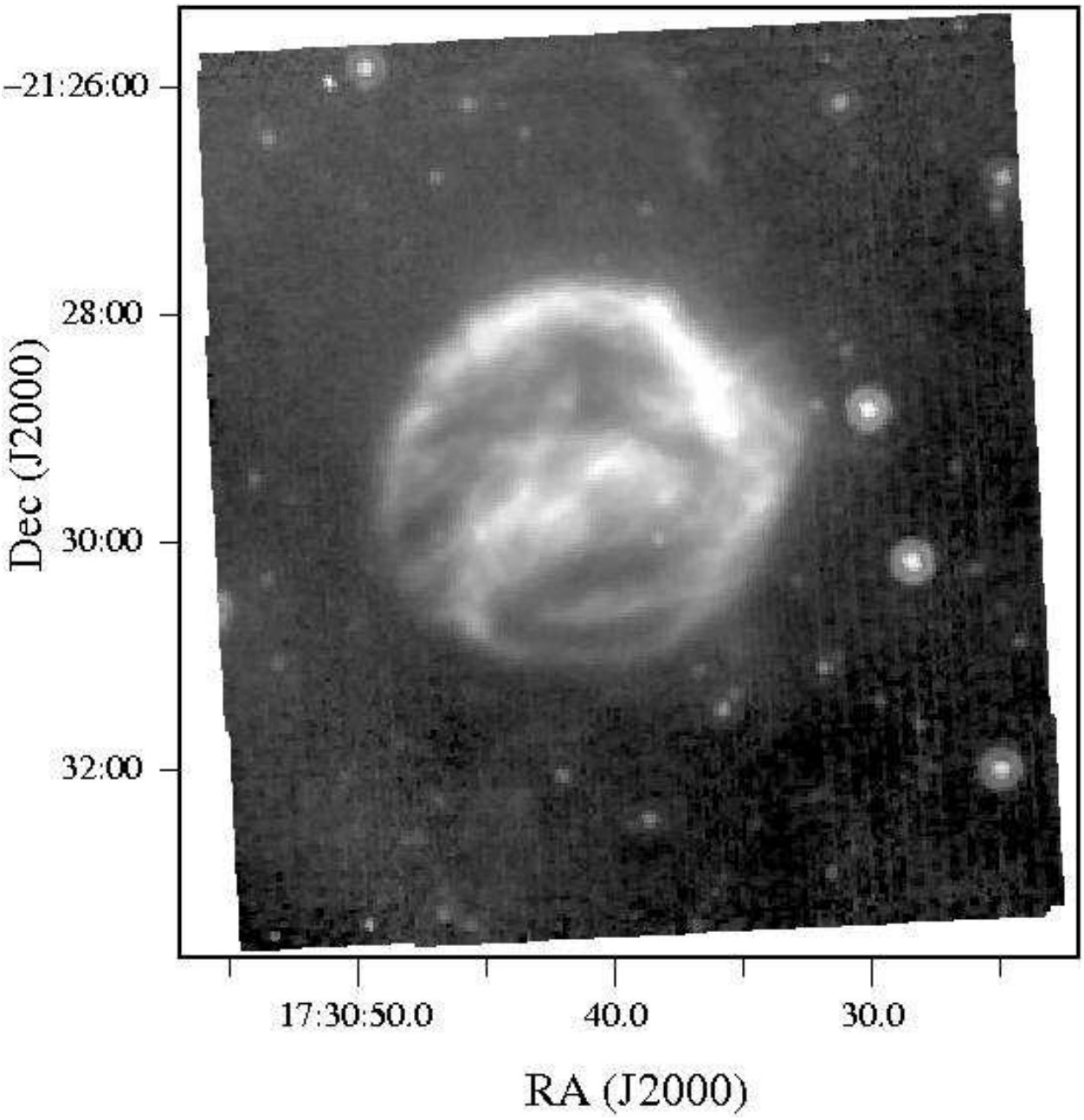
–21:26:00
28:00
30:00
32:00
Dec (J2000)
17:30:50.0
40.0
30.0
RA (J2000)

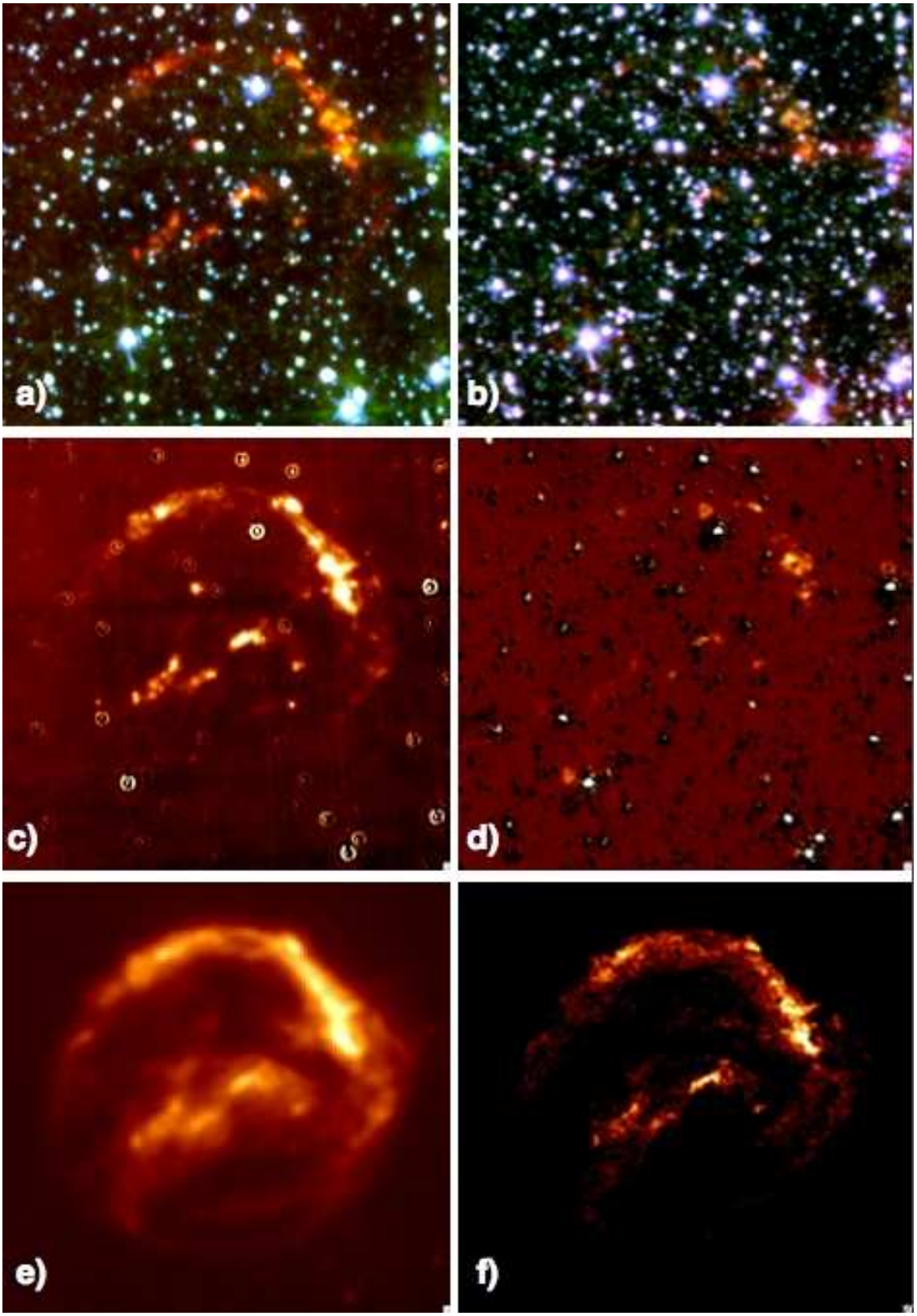
a)
b)
c)
d)
e)
f)

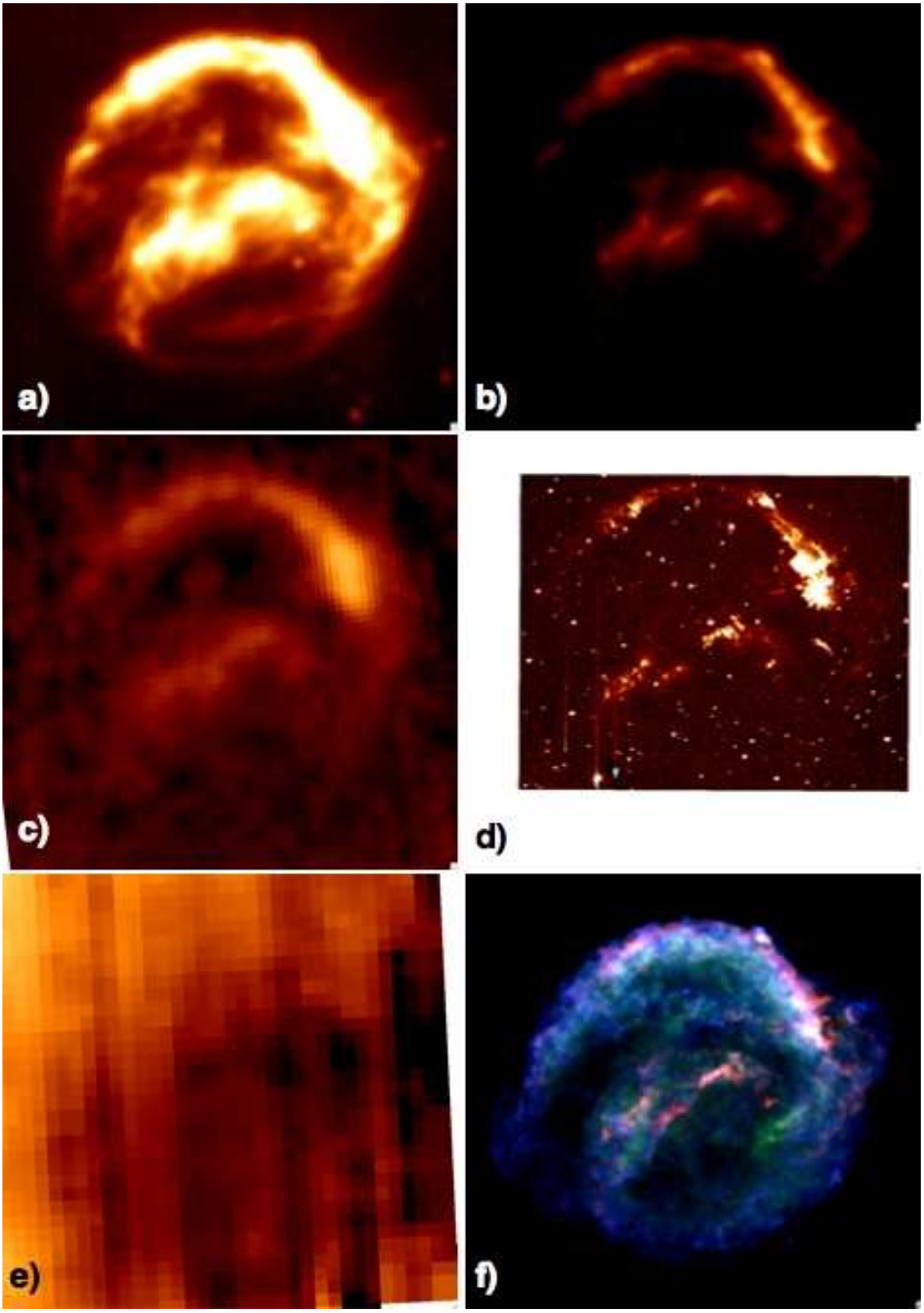
a)
b)
c)
d)
e)
f)

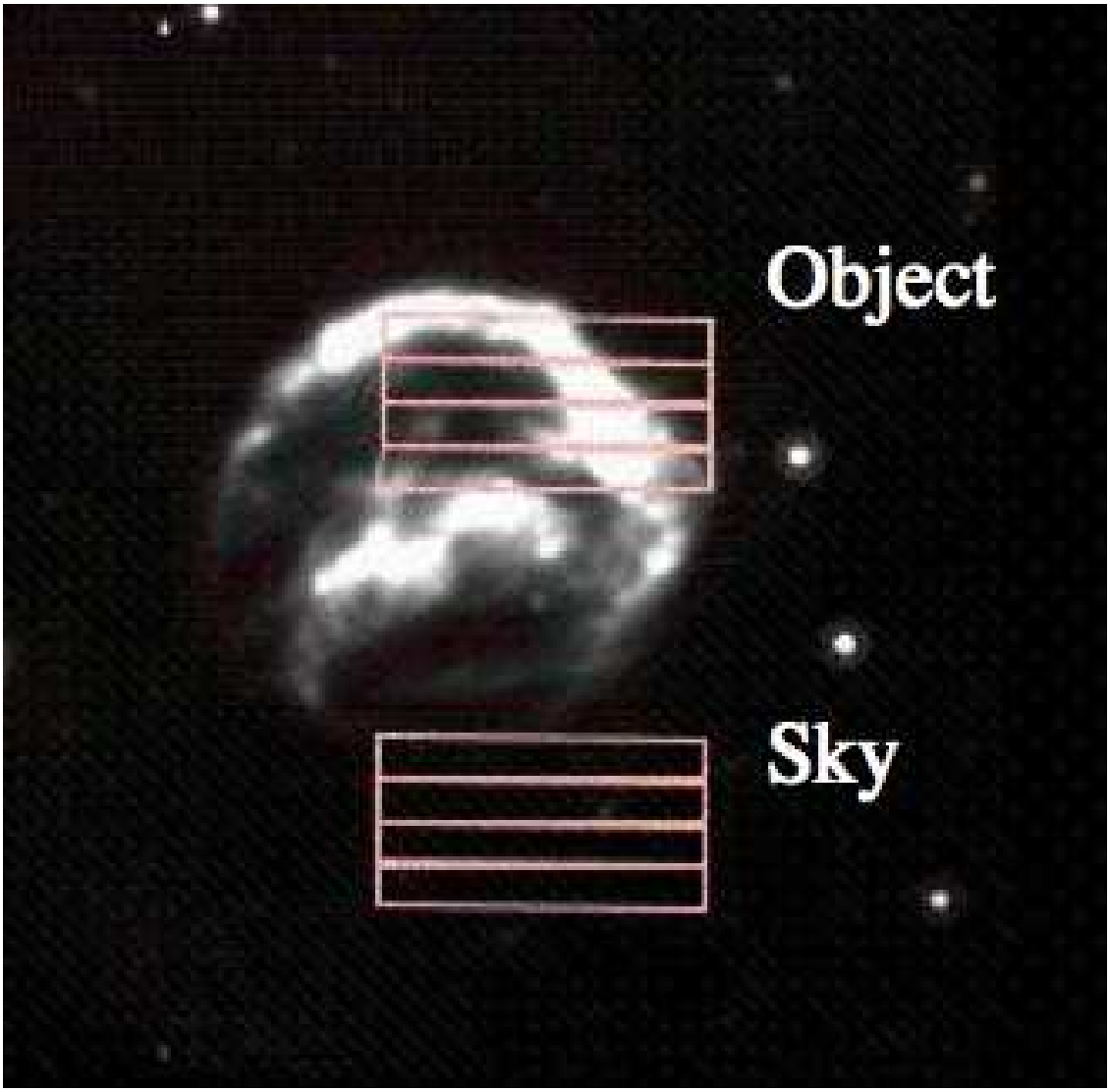
Object
Sky

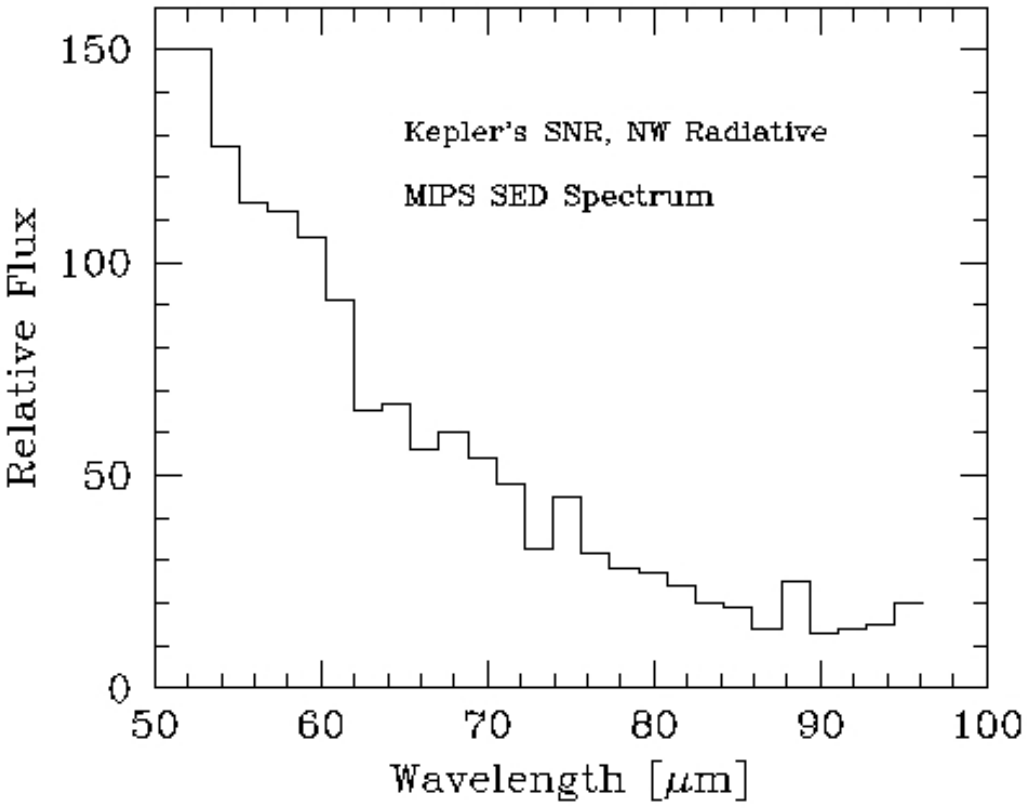
Kepler's SNR, NW Radiative
MIPS SED Spectrum
Relative Flux
Wavelength [μm]
0
50
100
150
50
60
70
80
90
100

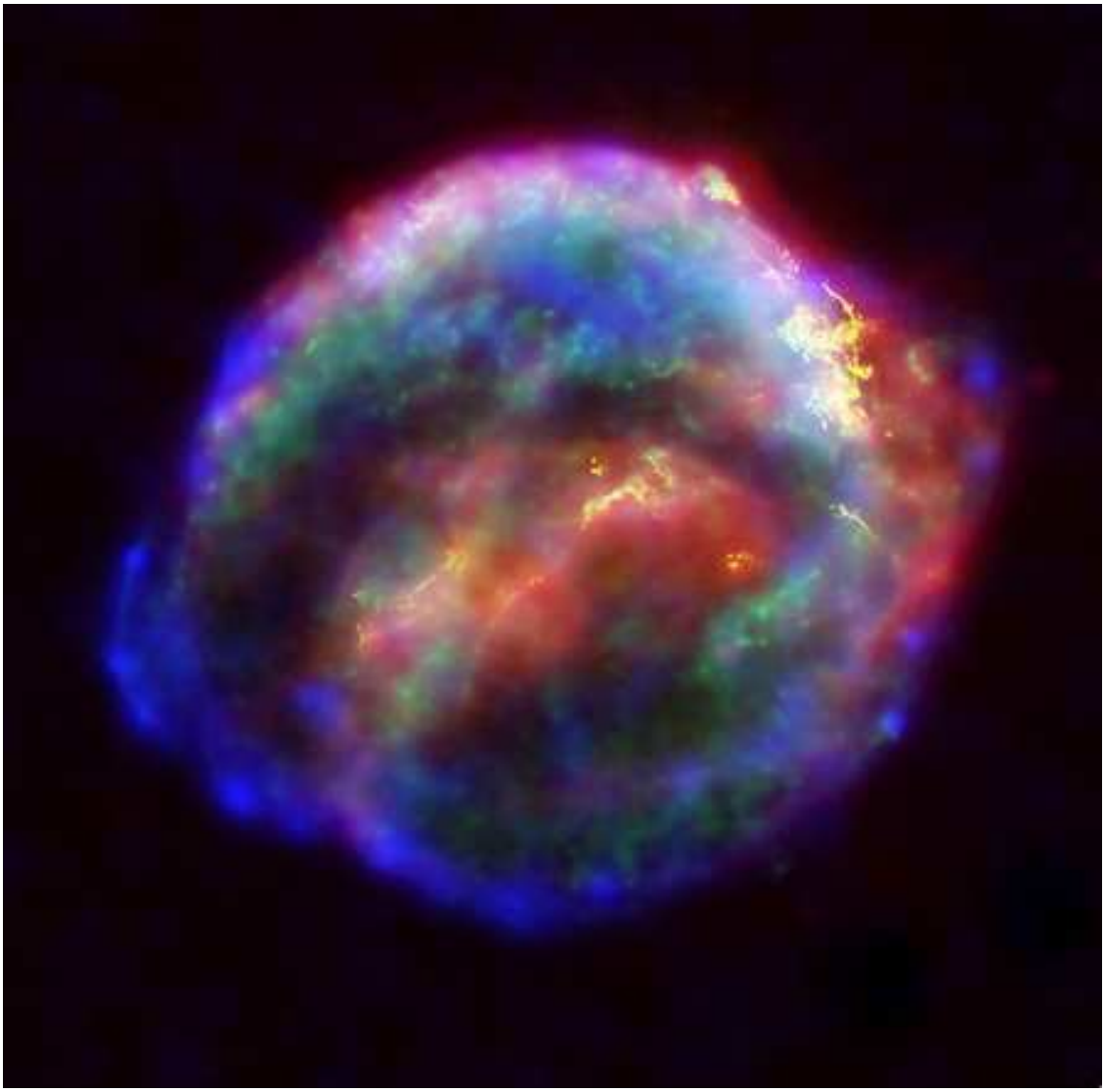

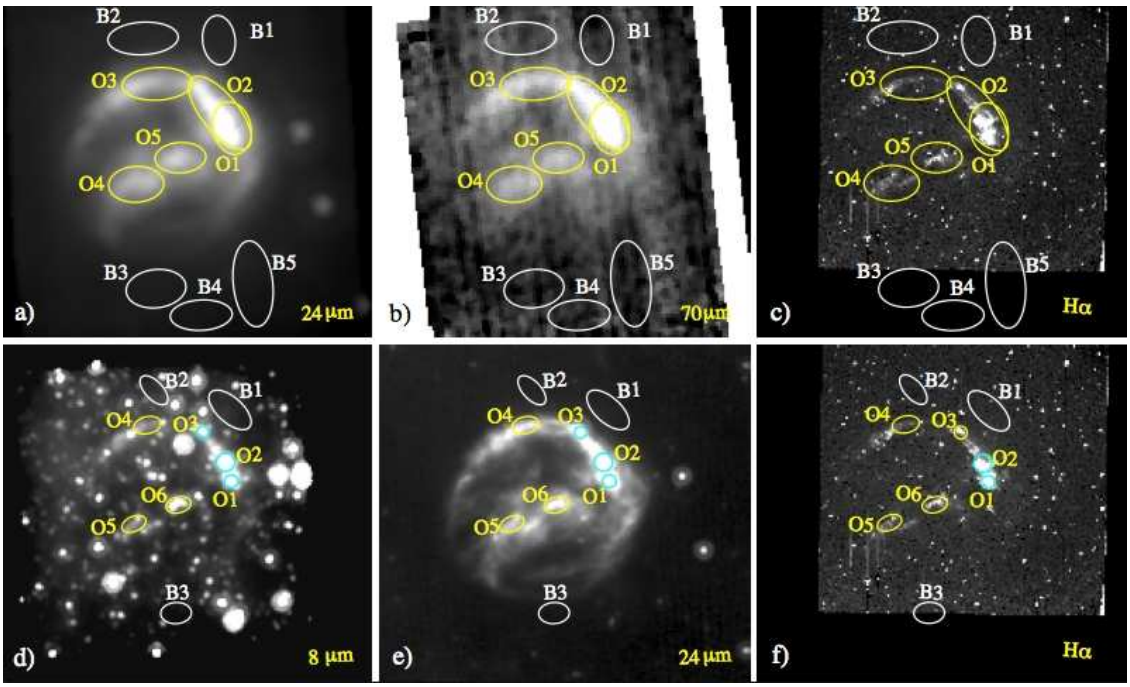
B2
B1
O3
O2
O5
O1
O4
B3
B4
B5
a)
24 μm
b)
70 μm
c)
Hα
O6
d)
8 μm
e)
f)

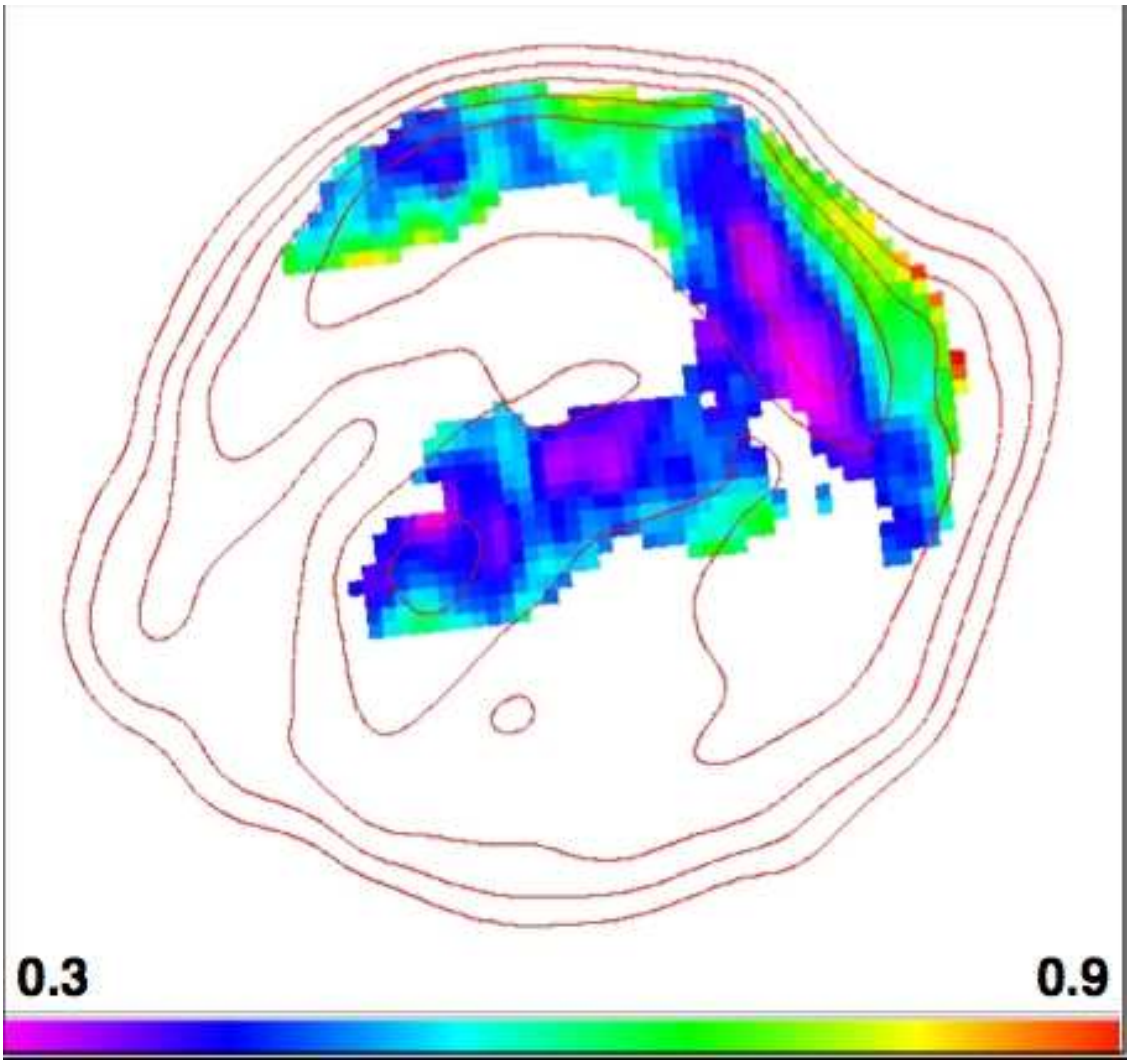
0.3
0.9

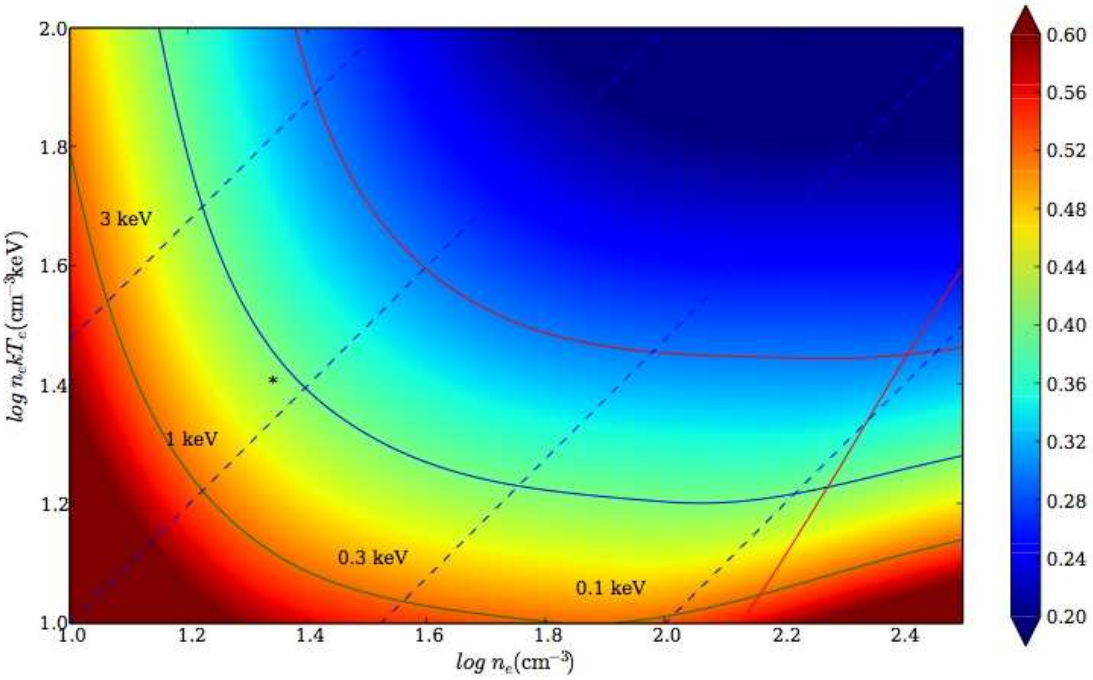
3 keV
1 keV
0.3 keV
0.1 keV
$log\ n_e kT_e (\mathrm{cm}^{-3}\mathrm{keV})$
$log\ n_e (\mathrm{cm}^{-3})$
2.0
1.8
1.6
1.4
1.2
1.0
1.0
1.2
1.4
1.6
1.8
2.0
2.2
2.4
0.60
0.56
0.52
0.48
0.44
0.40
0.36
0.32
0.28
0.24
0.20

Table 1. Aperture Parameters for Region Extractions[a]

Region	α (2000)	δ (2000)	Semi-Major Axis ($''$)	Semi-Minor Axis ($''$)	PA ($^\circ$)
24 μm to 70 μm:					
Object 1	17:30:35.76	-21:28:44.5	21.4	30.0	192.9
Object 2	17:30:36.73	-21:28:27.2	20.8	50.2	218.9
Object 3	17:30:41.81	-21:27:54.6	39.8	18.4	182.9
Object 4	17:30:43.51	-21:29:48.0	31.2	20.2	182.9
Object 5	17:30:39.93	-21:29:17.9	28.8	17.2	182.9
Background 1	17:30:36.82	-21:27:05.2	18.5	27.9	186.3
Background 2	17:30:42.96	-21:27:03.2	39.8	18.4	182.9
Background 3	17:30:41.91	-21:31:45.7	34.0	21.6	186.3
Background 4	17:30:38.24	-21:32:15.7	35.1	17.2	182.9
Background 5	17:30:34.05	-21:31:40.2	22.3	48.7	186.3
8 μm to 24 μm:					
Object 1	17:30:35.81	-21:28:55.0	7.2	7.8	93.2
Object 2	17:30:36.28	-21:28:33.7	10.2	10.2	0
Object 3	17:30:38.14	-21:27:59.7	7.2	7.2	0
Object 4	17:30:42.61	-21:27:51.8	9.6	15.6	103.2
Object 5	17:30:42.61	-21:27:51.8	9.6	15.6	103.2
Object 6	17:30:40.09	-21:29:21.8	9.0	14.4	103.2
Background 1	17:30:35.92	-21:27:34.5	29.4	14.4	138.2
Background 2	17:30:42.07	-21:27:12.3	10.2	20.4	43.2
Background 3	17:30:40.28	-21:31:23.9	12.0	17.4	93.2

[a]Refer to Figure 7 for region identifiers projected onto images.

Table 2 – MIPS 70/24 μm Regions Summary

Region[a]	Net 70 μm[b] Flux mJy	Net 24 μm Flux[b] mJy	70/24 Ratio
O1	778	2133	0.36
O2	1171	3125	0.37
O2 − O1	394	992	0.40
O3	412	1032	0.40
O4	349	886	0.39
O5	242	766	0.30

Notes: (a) Refer to Figure 7a-c for region definitions. (b) Net fluxes have been background-subtracted as described in the text.

Table 3 – MIPS 8/24 μm Regions Summary

Region[a]	Net 8 μm[b] Flux mJy	Net 24 μm Flux[b] mJy	8/24 Ratio
O1	10.4	409	0.025
O2	16.5	571	0.029
O3	6.9	242	0.029
O4	6.9	314	0.022
O5	5.4	228	0.024
O6	11.7	339	0.035

Notes: (a) Refer to Figure 7d-f for region definitions. (b) Net fluxes have been background-subtracted as described in the text.